Politecnico di Torino

Corso di Laurea Magistrale in Ingegneria Biomedica

Tesi di Laurea Magistrale

Use of DXA-based statistical shape models of the femur for hip fracture risk prediction.

Supervisors:
Dr. Terzini Mara, Supervisor
Dr. Aldieri Alessandra, Co-supervisor

Candidate:
Pagotto Federica, 279866

anno accademico 2021/2022

Abstract

Osteoporosis is a systematic skeletal disorder characterized by low bone mass and microarchitectural deterioration of bone tissue, with a consequent increase in bone fragility and susceptibility to fracture, affecting about 30% of post-menopausal women.
Nowadays, the main operational criterion to establish the presence of osteoporosis is based on the measurement of the areal Bone Mineral Density (aBMD) through Dual energy X-ray Absorptiometry (DXA). However, different studies have shown that nearly half of the subjects experiencing a low trauma hip fracture were classified as "low risk" according to the aBMD value.
To overcome this problem and improve fracture prediction, different studies have been conducted, ranging from the analysis of the parameters of Hip Structural Analysis (HSA) and Trabecular Bone Score (TBS), up to the use of QCT images for the creation of Finite Element (FE) models to predict the bone load to failure or for the development of three-dimensional statistical shape models, in order to identify fracture-prone features. Nonetheless, the main problem with the aforementioned analyses is that QCT is not routinely performed in a clinical environment.
In order to overcome this problem, in this work the possibility to build statistical models of DXA-derived proximal femur shapes is investigated, aiming at the hip fracture risk prediction in a post-menopausal Caucasian cohort. Fifty post-menopausal women, aged 55-90 years who had sustained a hip fracture were recruited as fractured cases, and for each case a post-menopausal woman matched with age, weight and height, was enrolled as control.
The patient-specific geometry of the proximal femur was extracted by performing a semi-automatic segmentation of the DXA images in which the femoral head was simplified as a circle and the lesser trochanter was not considered because not present in all DXA images. Subsequently, the patient-specific 2D femur shapes were given as inputs to Deformetrica, who allowed the extraction of the template, i.e. the mean anatomical shape, and of the so called moment vectors, which gather the patient-specific anatomical features. Then, the moment vectors were used to build Statistical Shape Models (SSMs).
Principal Component Analysis (PCA) and Partial Least Square (PLS) were adopted, leading to two distinct SSMs. While PCA maximized the variance found in the femurs anatomical features, PLS identified the modes maximizing the covariance between femurs anatomical features and the known patient-specific fracture status. Later, the identified modes were used for the implementation of logistic regression models for the prediction of the patients' fracture status, which were tested using a 10-fold cross-validation procedure.
The first five PCA modes and PLS modes were selected, which could explain at least 90% of the total shape variance. The predictive model with the first two, three, four and five PCA components used as predictors resulted in AUC values all settled between 0.59 and 0.62; instead, for the PLS components provided AUC values between 0.62 and 0.63. An AUC value of 0.73 was obtained using the gold standard aBMD.
In conclusion, the use of purely SSM does not seem to outperform the current gold standard for hip fracture risk prediction. The inclusion of Statistical Intensity Models (SIMs), built starting from the local BMD values of DXA images, might allow an enhanced fracture risk assessment.

Contents

List of Figures

List of Tables

List of Acronyms

ADC Apparent Diffusion Coefficient

AUC Area Under Curve

BMD Bone Mineral Density

BR Buckling Ration

DXA Dual X-ray Absorptiometry

ECM Extra-Cellular Matrix

FA Fractional Anisotropy

FE Finite Element

FRAX Fracture Risk Assessment Tool

FS Femoral Strength

HAL Hip Axial Length

HSA Hip Structural Analysis

MR Magnetic Resonance

NSA Neck Shaft Angle

OS Oxidative Stress

PCA Principal Component Analysis

PLS Partial Least Square

QCT Quantitative Computed Tomography

QUS Quantitative bone UltraSonography

RFI Risk Factor Index

ROC Receiver Operating Characteristic

ROS Reactive Oxygen Species

SA Sensitivity Analysis

SD Standard Deviation

SSM Statistical Shape Model

SSIM Statistical Shape and Intensity Model

SIM Statistical Intensity Model

TBS Trabecular Bone Score

WHO World Health Organization

ESOPO Epidemiological Study On the Prevalence of Osteoporosis

LDDMM Large Deformation Diffeomorphic Metric Mapping

1. Introduction

1.1 Skeletal system

The skeletal system [1] includes a set of bones, connected by joints, and different tissues, such as cartilage and ligaments. The most important features of this system and its components are:

- construct the framework of the body;
- protect vital structures;
- offer regions of anchorage to muscles and ligaments;
- participate in the formation of blood, through the bone marrow;
- participate in controlling the calcium and phosphorus content within the body.

The external surface of the bone, with the exception of joint surface covered by cartilage, is surrounded by a membrane of connective tissue, rich in blood vessels and nerve fibers: *Periosteum* [1]. It consists of an external fibrous layer and an internal osteogenic layer [1] and includes numerous blood vessels and lymphatics vessels, as well as nerves, which are responsible for the painful sensations after bones trauma.

After a macroscopic examination is feasible to take a look at two different tissues: *cortical bone tissue* and *cancellous bone tissue*. Cortical bone is a material with a density of 2 kg/dm^3; while the spongious bone has a density that varies among 0.15 and 1 kg/dm^3, it is also called trabecular because it is made up of bone tissue organized to form many girders, intertwined in various random ways. These trabeculae are particularly oriented according to the directions of transmission of the stresses to which the bone is submitted. Thanks to this complicated architecture, the spongy bone makes the bone more elastic and much less fragile: in osteoporosis, the growth in fragility isn't always because of the thinning of the cortical bone, as for the loss and the rarefaction of spongy trabeculae, which "empties" the bone making it structurally weaker [2].

The principal structural components of bone tissue [3, 4] as an entire are the Extra-Cellular Matrix (ECM) and the bone cells. A bone matrix is made up, in dry weight, of about 35% of collagen and proteoglycans, while the remaining 65% of hydroxyapatite (a calcium phosphate crystal). These are responsible for the principal functional characteristics of the bone: collagen provides deformability to the bone matrix, while the mineral components give the matrix resistance to compression.
Bone cells such as osteoblast, osteoclast and osteocytes are responsible for the metabolic activity of the bone. In fact, bone [3] is a metabolically active structure and it is subjected to a process called *bone turnover* (explained in figure 1.1), which allows a daily turnover of its ECM in order to guarantee the structural integrity of the skeleton and the blood calcium homeostasis. This latter is carried out by *osteoclasts* responsible for the degradation of dysfunctional bone, *osteoblasts* carry out the biosynthesis of the new bone to be replaced and the *osteocytes* that form a three-dimensional network interconnected throughout the bone tissue by acting as a mechanosensor that monitors mechanical stress within bone tissues and reacts to changes in the amount and direction of load applied to the bones. This process is fundamental because it allows to regulate plasma levels of calcium and

[1] The osteogenic layer is made from osteoblast cells (responsible for bone formation), osteoclasts (responsible for bone resorption) and osteochondral progenitor cells.

phosphorus, strengthen bone tissue in response to appropriate stimuli and restore stress microfractures.

Under optimal physiological conditions, bone resorption occurs in about 10 days and bone formation takes about 3 months. Up to 20% of the skeleton can be replaced by remodeling it every year. In conditions of metabolic equilibrium, the amount of reabsorbed bone and new bone is equal, but when the amount of absorbed bone is greater than the newly formed one, first a condition of osteopenia is established, and when the amount of minerals falls below a certain threshold, a condition called osteoporosis.

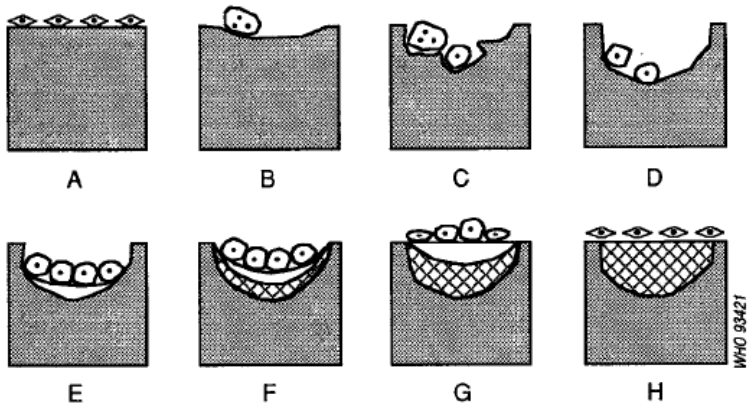

Figure 1.1: *Trabecular bone surfaces are protected by lining cells or osteoblasts (A). Firstly, osteoclasts are interested in a quiescent bone surface and burrow a resorption cavity (B, C). Mononuclear cells clean off the resorption cavity (D), which is the following site of the attraction of osteoblasts, which synthesize an osteoid matrix (E). Continuous new matrix synthesis (F) is followed by calcification (G) of newly formed bone. In the end, lining cells overlap the trabecular surface (H). [5]*

1.2 Osteoporosis

Osteoporosis [6] is a skeletal disorder characterized by a compromised bone strength, which causes an increased risk of fracture, particularly of vertebrae, femur and wrist even because of minimal trauma. In general, osteoporosis manifests with advancing age, influences about 30% of post-menopausal women. Different studies exhibit that the fracture risk, in osteoporotic subjects, can be decrease by 70% with a protective bone therapy [2], which has a low rate of adherence for the high cost [8]. Other studies report that the intervention through physical activity may be a better alternative treatment. The aim of this type of therapy is to improve the bone's ability to withstand a significant degree of load, including weight lifting, plyometrics and other high-impact activities. It has also been assessed that swimming, even if it is considered a low-load sport, can affect the density of the lumbar vertebrae of pre-menopausal swimmers. This can also be a good strategy for the clinical prevention and treatment of osteoporosis [9].

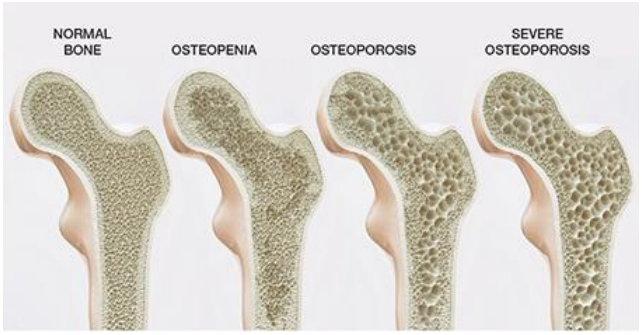

Figure 1.2: *Representation of different stages of osteoporosis*

According to [10], bone mass is the major measurable factor for determining the risk of osteoporotic fractures, but it is necessary to combine it with independent risk factors like ethnicity, age, low body mass index or sex. In fact, in [11, 12] it is stated that women are twice as likely to fracture as men. For example, women have approximately a five times bigger risk of maintaining a forearm fracture than men but much less than two times of the risk sustaining a backbone fracture. The principal reason is the lost bone density, which is determined by menopause and by its change of hormonal concentration. In addition, the prospect of women's life is longer than men and so they have an extended period of reduced bone density. On the contrary, men have a higher assessment of fracture-related mortality than females, perhaps linked to more elevated rates of comorbidity.

The most common osteoporotic fractures comprise vertebral fractures, fractures of the forearm, hip fractures, and proximal humerus fractures. Hip fractures induce acute pain and lack of function, and nearly always result in hospitalization where recovery is gradually and rehabilitation is often undone. Vertebral fractures might also additionally cause acute pain and lack of function but may also take place without critical symptoms; this type of fracture frequently recur and the resulting disability increases with the number of fractures. Distal radial fractures also guide to acute pain and lack of function, but active recovery is usually adequate or superior [13].

[2] Protective bone therapy is a treatment that uses Bisphosphonates [7], which are a category of drugs that control the loss of bone density. Evidence shows that they decrease the risk of fracture in postmenopausal women with osteoporosis.

1.2.1 Etiopathogenesis

According to its etiology, osteoporosis is distinguished in primary and secondary osteoporosis [6, 14].

Primary osteoporosis is characterized by the absence of other clinical conditions capable of determining the quantitative and qualitative skeletal damage which, in turn, is at the origin of reduced bone resistance and increased susceptibility to fractures [15]. This includes: postmenopausal osteoporosis (Type I), involutive (senile) osteoporosis (Type II), and idiopathic osteoporosis, which have some distinctive features regarding the age of onset, severity and reversibility of bone damage, and prevailing fracture locations.
Osteoporosis type I (post-menopausal osteoporosis) affects women within twenty years since menopause, recognizes estrogen deficiency as a fundamental pathogenetic mechanism and is characterized by fractures in skeletal sites that are rich in trabecular bone tissue, such as the vertebrae and the distal radius. One of the hypotheses about how estrogen acts on bone density is the capacity of this hormone to preserve bone from Oxidative Stress (OS)[3]. Practical studies have shown that OS is a salient factor in bone remodeling [14]. The results were further demonstrated by case-control studies, in which OS was represented by a high level of F2-isoprostanes in the urine and a low grade of antioxidant enzymes in the blood, along with decreased bone mineral density and improved risk of osteoporosis. In addition to this factor, there are others that can increase the risk, such as: smoking, excessive thinness, a sedentary lifestyle or even an excess of protein, sodium and caffeine.
On the contrary, **osteoporosis type II** (senile osteoporosis) affects both sexes with increasing age and reflects hormonal changes in the bone tissue. In this case, fractures typically involve sites composed of both cortical and trabecular bone tissue, such as the femur, humerus, tibia and pelvis.

Secondary osteoporosis is caused by various types of diseases that can, directly or indirectly, lead to a reduction in skeletal resistance. The recognition of the forms of secondary osteoporosis is of extreme importance since, if properly diagnosed and treated, it is, in most cases, reversible. If osteoporosis therapy is prescribed to a patient who has not been diagnosed with a secondary form of osteoporosis, it may lead to a failure to respond to the therapy or even damage in terms of bone mass loss and increased risk of fracture.

[3]OS is developed as a consequence of the inadequate activity of the endogenous antioxidant protection system against Reactive Oxygen Species (ROS) [14]

1.2.2 Epidemiology of osteoporosis and fragility fractures

In the world, there are 75 million people affected by osteoporosis, mainly in Europe, U.S.A. and Japan [16]. The Surgeon General report on bone health and osteoporosis [17] announced that in 2004 osteoporosis has affected more than 8 million females and 2 million males in the United States, in addition to 34 million individuals with low bone mass. In 2000, nearly 4 million osteoporosis fractures were recorded in Europe, of which almost 1 million were at the hip. This kind of fracture occurs more frequently in the elderly after a fall [18], a result of decreased bone strength integrated with age and an improved chance of falling. Among the osteoporosis fractures, this is classified among the most severe, with an increase in mortality of 10-20% in the year following the fracture [19]. Similarly, fractures of the proximal femur are considered particularly devastating due to the numerous aftermath they generate in terms of persistent discomfort and limited physical mobility [20].

Osteoporotic fractures also guide to a considerable decrease in the level of independence due to disability and, therefore, to a greater need for long-term care. From this point of view, the costs of osteoporosis, together with pharmacological interventions, were documented to be equal to 37 billion euros in 2010 [13], provided for 66% is for the treatment of incident fractures, 5% for pharmacological interventions and 29% for long-term fracture care. While 54% of total costs represent only the hip fractures[12].

In Italy, the capacity of incidence of osteoporosis and osteopenia was examined through the Epidemiological Study On the Prevalence of Osteoporosis (ESOPO) study [6]; which showed that among women the incidence of the first and second pathology was respectively equivalent to 44.7% and 18.5%, while in the male sex the corresponding rates were 36% and 10%. Looking at the Italian incidence of fractures in men and women (Table 1.1), an exponential increase in the incidence can be observed, with much higher rates in women than in men.

Table 1.1: *Prevalence of osteopenia e osteoporosis*

	Normal	Osteopenia	Osteoporosis
Women			
40-49 age	55.7%	39.9%	4.4%
50-59 age	41.9%	46.4%	11.7%
60-69 age	24.4%	47.6%	28.0%
70-79 age	15.0%	43.1%	41.9%
Man			
60-69 age	55.2%	36.3%	8.5%
70-79 age	50.9%	35.8%	13.3%

We can therefore observe that osteoporosis incidence grows with aging and, due to the raised longevity of the population, it is expected to grow dramatically [6].
In Europe, the percentage of the elderly over the entire population will increase by 33% over the following 25 years [11] and in Italy, where it is approximate that 3.5 million females and 1 million males suffer from osteoporosis, the percentage of people over the age of 65 should increase by 25% over the next 20 years, reasonably leading to a proportional increase in the incidence of osteoporosis [10]. In 2017, a total of 560,000 fractures were registered in Italy, with a cost related to the health system of 9.4 billion euros. 20% of these, being characterized by hip fractures, involved a cost of about 6 billion euros [13].
These numbers are expected to steadily increase over time: in this light, early diagnosis, prevention and treatment of osteoporosis turn out to be extremely important [21].

1.3 Methods of diagnosis

Nowadays densitometric techniques are able to diagnose the early phases of osteoporotic deterioration, differentiate patterns of bone alteration, predict the risk of fractures, which define a strong factor related to morbidity and also mortality of these patients, and address both therapy and follow-up [22]. These techniques are the safest and most useful for the estimation of mineral content and bone mass. Several techniques are proposed to carry out this density quantification [6, 16, 23, 24].

- **Quantitative bone UltraSonography (QUS)**:The QUS is a moderately simple, cheap method, easy to implement, transportable, that does not use ionizing radiation and makes it well tolerated by patients. This type of examination provides two parameters (velocity and attenuation) which are indirect measures of bone mass and structural integrity and is measured predominantly at two sites, the phalanges of the hand and the heel. The combined use of ultrasonographic parameters and risk factors improves the prediction of fracture risk. In addition, recent studies have shown that by ultrasonographic measurement it is possible to obtain other complementary details such as the allocation of the mineralized matrix within the bone (connectivity or the thickness of the trabeculae), the different resistance to the load of the bone tissue as a function of the trabecular orientation.
- **Traditional radiography**: The main task of the traditional radiological study is to make an early diagnosis of osteoporosis fractures in the influenced sites. In particular, the radiologist's task is to detect the features of bone resorption and to try to quantify the loss of bone by estimating the thickness of the bone cortical, the decline of trabecular beams and, in the case of the spine, the majority of vertical trabecular systems in answer to the modified biomechanical stimulus with the striated appearance of vertebral bodies. Moreover, traditional radiological methods have high inter-operative variability, which restricts their clinical applications in different centers. For this reason, it is used in conjunction with other different bone densitometry techniques (e.g DXA, QCT) that permit obtaining a more objective quantitative measurement of the mineral bone present in a given district, for screening and follow-up of osteopenic patients.
- **Magnetic Resonance (MR)**: MR is a non-invasive investigative device that provides information on how water is distributed to biological tissues. Two parameters can be obtained: the *Apparent Diffusion Coefficient (ADC)* and the *Fractional Anisotropy (FA)* that permit analyzing the microscopic system of the tissues within the water diffuses. At the ends of the long bones, the bone consists of trabecular bone formed by a solid matrix with many interconnected pores, which are filled with bone marrow consisting mostly of fat and water. By calculating the parameters ADC and FA it is possible to obtain information about the microstructural state of the bone tissue. In fact, with the development of osteoporosis, there is an addition of the fat in the bone marrow, which reduces the space in the pores within which the water spreads, reducing its diffusion coefficient, and degradation of the bone matrix, with an increase in the average diameter of the pores, which results in an increase in water diffusion coefficient due to an increase in the interstitial area between the fat and the wall of the bone matrix.

- **Quantitative Computed Tomography (QCT)**: QCT is a non-invasive technique that estimates the actual density of bone tissue in a given volume, in mg/cm^3. It is an imaging method that, in addition to bone density, can provide information on the structure of the skeletal segment examined. There is a high-resolution QCT, with a spatial resolution below 1 mm, that denotes the starting point of structural analysis analyses, allowing to quantify the changes in the microstructure of the trabecular bone and its mechanical strength. In particular, the approach makes possible to analyze the contiguity of the trabeculae, the thickening, the distance, the spatial disposition and the structure of the trabeculae (understood as a measure of anisotropy).
- **DXA**: the DXA is the current gold standard that permits an accurate measure of the bone mass and, in particular, the bone mineral density in g/cm^2 of the projected bone surface. For the World Health Organization (WHO), the densitometric diagnosis of osteoporosis is established on the DXA evaluation of the bone mineral density defined by T-score, that is a Standard Deviation (SD) compared to the average of healthy adults of the identical sex. This technique is discussed in detail in the next section.

1.3.1 DXA, Dual X-ray Absorptiometry

The DXA, also called densitometry or dual energy X-ray absorptiometry, represents the current gold standard for the diagnosis of osteoporosis and, therefore, the risk of fracture. This is a radiological technique that estimates the total bone mass index, called Bone Mineral Density (BMD) [25]. In particular, the presence of osteoporosis is estimated using the T-score [18], which represents the distinction, in terms of standard deviation (SD), between the bone density of a given subject and that of a young standard population of the same sex (Eq. 1.1).

$$Tscore = \frac{BMDpatient - BMDaverageoftheadultpopulation}{standarddeviationoftheadultpopulation} \tag{1.1}$$

Based on the WHO's criteria, a patient with a T-score of -2.5 to the hip or spine is supposed to be suffering from osteoporosis [26] (Tab. 1.2).
Another significant value represented by DXA is the Z-score, which varies from the T-score only because in this case the patient's BMD is compared with a population of peers of the subject (Eq. 1.2).

$$Zscore = \frac{BMDpatient - BMDaverageofthepopulationofthesameage}{standarddeviationofthepopulationofthesameage} \tag{1.2}$$

A Z-score of less than or equal to -2.0 is defined as "low bone mineral density by chronological age" or "below the expected age threshold"; for values above -2.0, "values within expected age limits" [16] (Tab. 1.3).

Table 1.2: *WHO's diagnostic thresholds for BMD at the spine, hip or distal forearm*

Category	**T-score-based definition**
Normal	$+2.5 >$ T-score $>$ -1
Osteopenia	-1 $>$ T-score $>$ -2.5
Osteoporosis	T-score $<$ -2.5
Severe osteoporosis	T-score $<$ -2.5 with one or more brittle fractures.

Table 1.3: *Thresholds for the diagnosis of osteoporosis in case of early menopause or men under the age of 50.*

State	**Z-score**
Normal	-2 $<$ Z-score
Osteoporosis	-2 $>$ Z-score

The statement of densitometry was to quantify the bone contrast and to calibrate it in terms of the bone mineral that produces the contrast. The DXA method simplifies the issue by using the principle of differential attenuation at two X-ray energies to provide an image in which only inorganic mineral [27, 28], is present. Depending on the tools used, those photons may be obtained by the use of two mechanisms. In some cases, the generator emits alternating radiation of high (140 kVp) and low ($70-100$ kVp) kilovoltage as it moves through the surface of the body to be examined. In others, the generator emits a continued beam while a filter separates high energy (70 KeV) from low energy photons (40 KeV) [29].

The effect of this attenuation is visible in Figure 1.3 where a conventional DXA image is plotted as a topographic surface rather than a gray-scale picture. Pixels in the DXA image are calibrated in terms of inorganic bone minerals represented in units of g/cm^2. Organic collagen, which binds the mineral together and is essential for the strength of the material, is removed. A pixel value of 1 g/cm^2, for example, is equal in thickness to a layer of 1 g of hydroxyapatite distributed over an area of 1 cm^2. The values characterize [27] the thickness of the mineral counted along the path to a point, and the units are a consequence of the attenuation physics. In fact, a DXA image does not tell us anything about how the mineral is distributed along the projection path; therefore, it cannot be used to conclude tissue mineralization or porosity [30]. The contemporary DXA software effectively implements the original mineral contrast idea by evaluating the average contrast (thickness) in a region comparable to a box placed on a reproducible skeletal place (figures 1.4). After excluding values below a certain threshold, pixels within the region are averaged to obtain BMD, the average thickness of a mineral layer after removing all other materials [27, 30].

Although DXA provides an accurate planar representation of BMD, it is limited by its two-dimensionality and does not represent the spatial shape or distribution of the bone mass [25].

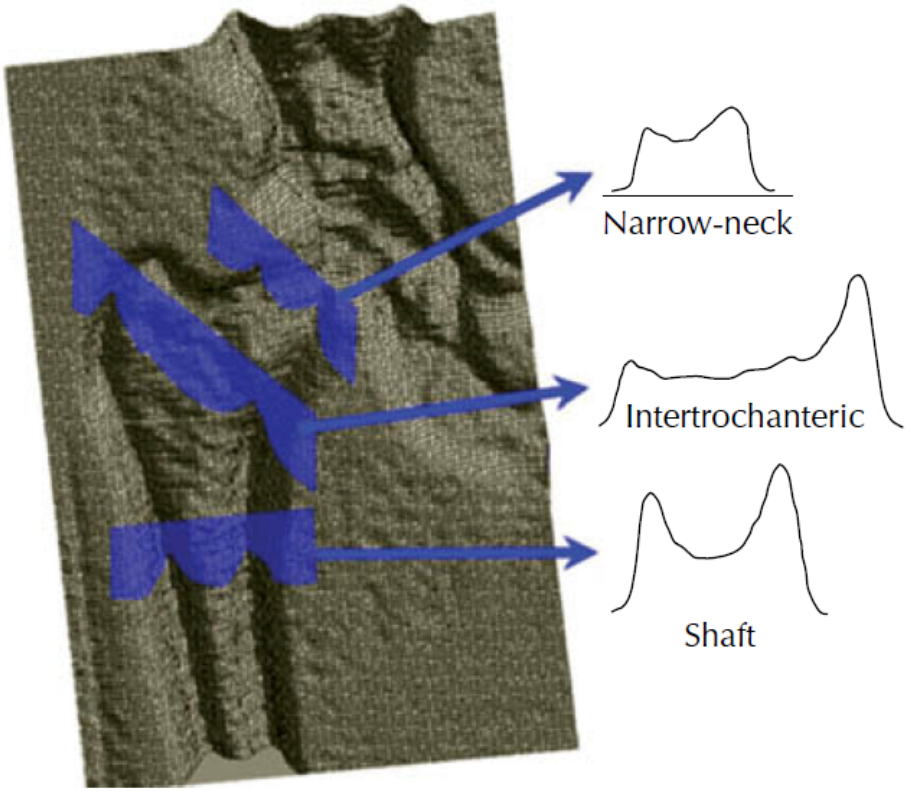

Figure 1.3: *A traditional DXA scan of the hip was plotted as a topographic map displaying the removal of all soft tissues within and across the bone mineral. The corresponding profiles from single lines of pixels are shown to the right [27].*

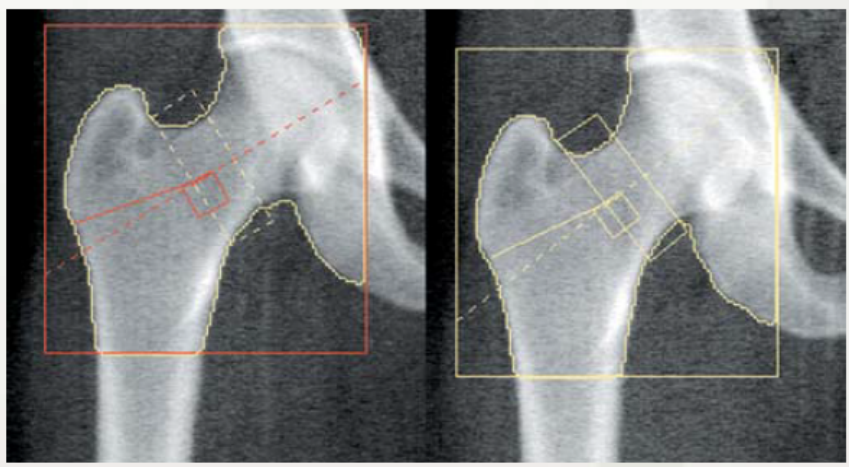

Figure 1.4: *An example of geometric model of the proximal femur built on a DXA scan.*

1.4 Assessment of fracture risk

Due to growing global life expectancy, the incidence of hip fractures is expected to grow 3.5 times by 2050, growing to a total of 6.26 million [31] osteoporotic subjects; this underlines the urgent need for a precise indicator of fracture risk.

Currently, the gold standard for the classification of a patient is the T-score deriving from the DXA. The accuracy of BMD measures using DXA to predict osteoporotic fractures is similar to using blood pressure measurements for predicting stroke [32]. The performance of BMD is moderate [33, 34], with about half of the people affected by fracture having non-osteoporotic T-score ranks [35]. It can therefore be said that the predictive interpretation of BMD is not sufficient to evaluate the risk of fracture [33].

Therefore, in order to identify clinically possible geometric features of the femur, many authors focused on improving fracture prediction.
On the one hand, efforts were put into identifying geometric characteristics to the predisposition to fracture of the proximal femur [27, 36–38]. Commonly evaluated considering the parameters of Hip Structural Analysis (HSA) and Trabecular Bone Score (TBS).
The first one (HSA) are geometric variables [27] that describe the precise geometry of the proximal femur and are extracted from the images DXA routine, which could be easily incorporated into clinical decision-making to sustain fracture risk based on T-score [39]. In addition, in different investigations [4, 40, 41] it was observed that the central HSA parameters involved in the optimal regression models as predictors of the Risk Factor Index (RFI) and Femoral Strength (FS) were the Buckling Ration (BR) at the narrow neck and Shaft, together with the Neck Shaft Angle (NSA). However, the improvement in HSA-based risk prediction over T-score is hampered by the fact that parameters derived from HSA [18] (1) define discrete measures incapable to describe the femur shape as a whole, (2) are highly related and (3) are connected to BMD.
While TBS [42, 43] give additional information about the trabecular micro-architecture quality through one parameter obtainable from a vertebral DXA image, processed by analyzing the pixel intensity variations throughout it.
On the other hand, the use of Finite Element (FE) evaluation has been proposed as a powerful and dependable calculation tool capable of fully estimating the risk of fracture [44–46]. 3D models of computed tomography (QCT) based on finite elements (FE) would enable the patient's specific three-dimensional geometry and material properties to be reliably and comprehensively reproduced, as well as the load distribution [18]. However, QCT is not routinely performed for osteoporosis diagnosis purposes, as it uses high doses of radiation.
This is why the role of 2D FE models developed from DXA images has also been investigated. The results of the model [39] have been shown to potentially improve the estimation of fracture risk, bringing additional information regardless of the BMD.

A further idea is to use the Fracture Risk Assessment Tool (FRAX) [5, 47, 48] which computes the 10-year probability of a major osteoporotic fracture combining together the BMD measurement at the femoral neck with the clinical risk factors in order to identify the patients at greater risk and assist treatment decisions. Yet, a considerable part of the patients facing a hip fracture is not considered at high risk even when BMD information is combined with epidemiological models such as FRAX, which would suggest the need to find more accurate practices to estimate fracture risk [4].

Statistical models have been introduced in recent decades to further improve the prediction of fracture risk; in particular Statistical Shape Model (SSM), Statistical Intensity Model (SIM) and Statistical Shape and Intensity Model (SSIM).
The first model (SSM) was introduced to examine the associations between the overall morphometric variations of the femoral form of an input cohort and the incidence of fractures [18, 49]. Basically, given a set of training images, the statistical modeling of the form allows the development of a linear model able to describe any new shape as the sum of an average and a weighted linear combination of independent modes of variation identified within the population [4]. As stated by Golland et al. [50], there are two essential features of the form descriptors that can greatly influence the quality of statistical models. One factor is related to the sensitivity of the model to image noise and the other concerns its ability to align all shapes in a common coordinate system [51], which largely determines the final performance of previous models of learned form. Despite providing information on the shape, the SSM approach does not take into account the density distribution within bones, the other crucial determinant of bone resistance. For this reason, another type of model was introduced, called statistical models of intensity (SIM), which are able to describe the intensity of pixels of the image of any new image according to the same scheme [4, 18]. It has been shown, [52] that the combined use of these two models represents a powerful tool for reconstruction and classification. These models (SSIM) are similar to SSM models but also include intensity information, which allows additional clinical benefits, such as estimating potential risk factors for individuals with osteoporosis [18] and helping in the task of distinguishing bone deformities from bone fractures.
Generally, however, the construction of SSIM requires longer calculation times and larger computer memory requirements [53], as it is necessary to establish the correspondence not only on the surface of the shape but also within the volume.

1.5 Aim of the Thesis project

This thesis will focus on the construction of statistical models of the femur shape, built starting from the DXA images of a population of 100 post-menopausal Caucasian women, with the aim of investigating the potential of such models in improving the prediction of the risk of fracture of the femur.

2. Materials and methods

2.1 Study population

This study was conducted on a cohort of 100 Caucasian female subjects aged between 55 and 90 years and in menopause for at least 5 years, treated at the University of Sheffield, England. The group consisted of 50 female subjects in whose 90 days prior to the test they had suffered a hip fracture, due to low-energy trauma, and 50 non-fractured subjects matched in term of age, height and weight were recruited as control group. Details of the cohort are extensively reported elsewhere [54]. Due to incomplete data, 4 subjects were not considered from the analysis, so 48 fracture patients and 48 controls patients were left.

For each subject constituting the cohort, a proximal femur DXA image was available (acquired with a system Discovery DXA, Hologic, Waltham, MA, USA). For patients who suffered a fracture, the contralateral femur was considered for analysis, assuming that the two femurs showed similar characteristics in terms of pathological form or subject to fracture and density (no patients had pathologies such as bone tumors or dysplasia).

2.2 DXA-derived data pre-processing

The whole methodological pipeline here presented will be base on DXA images. The aim was to investigate the potential of statistical models derived from the standard imaging technique used in osteoporosis in improving the prediction of the risk of fracture of the femur.

First, the external profile of the proximal femur was extracted from the DXA images. The extraction was based on the use of a semi-automatic interactive segmentation, through the software Matlab (Matlab R2019b, The Mathworks, Massachusetts, U.); in which the change of level of gray of the DXA image was evaluated. For convenience, the head was assumed as a circle and the lesser trochanter was excluded as it was not visible in many images (figure 2.1(a)).

Then, an optimization of the edge of the femur was made, the steps were: (1) contour smoothing to remove roughness, (2) scaling, (3) contour translation and (4) rotation resulting in alignment to their shaft axis. Images are now ready to be used as input for Deformetrica (figure 2.1(b)).

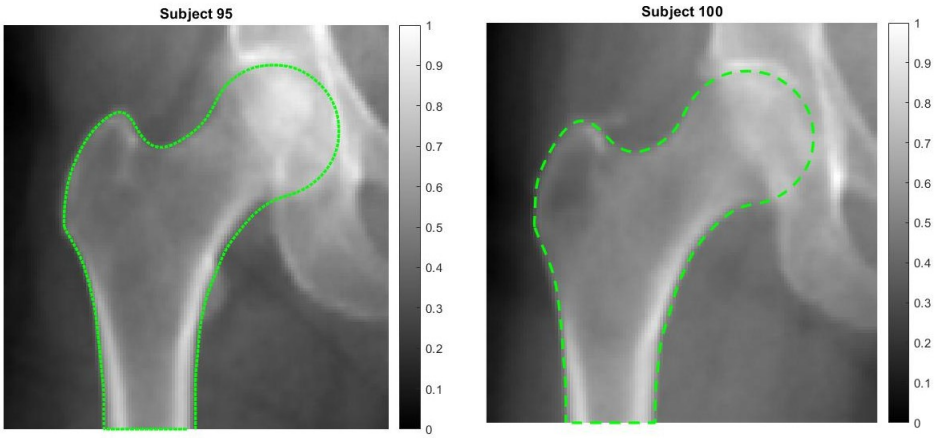

(a)

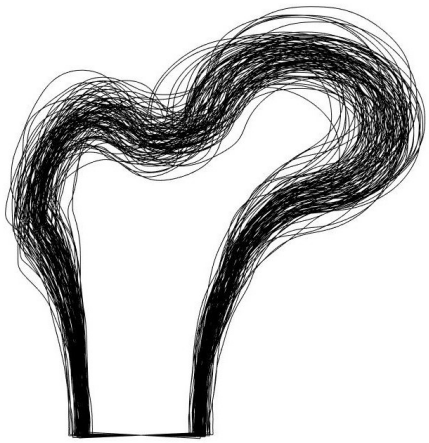

(b)

Figure 2.1: *(a) Example of two femur external profile. (b) Patient-specific two-dimensional profiles given as input to Deformetrica after the alignment procedure.*

2.3 Deformetrica

The starting point to carry out the statistical analysis of the shape, was based on the use of an open-source code called Deformetrica (http://www.deformetrica.org/), developed by Durrleman and his collaborators [55, 56]. This code was based on a specific instance of Large Deformation Diffeomorphic Metric Mapping (LDDMM) based on the control point and to represent and describe shapes it didn't need landmarking using mathematical currents.
The main idea of current was to probe shapes by vector fields, $w \in W$ across a surface S (or curve L); where W is a vector space created by a Gaussian kernel K_w with width λ_w[1]:

$$K_w(x,y) = exp\Big(-\frac{|x-y|^2}{\lambda_w^2}\Big) \tag{2.1}$$

[1]This width is a critical hyperparameter of any deformetrica run

For each point of the surface (or curve) it was possible to define a Dirac delta current ($\delta_{x_k}^{a_k^i}$), oriented through the normal (or tangent), and the surface could be approximated by a finite sum (Eq. 2.2), since the surfaces (or curves) can be represented with discrete meshes.

$$S^i = \sum_k \delta_{x_k}^{a_k^i} \tag{2.2}$$

After modelling the input forms with currents, the forward approach [57] was used to calculate the model $\bar{T}$, which represented the average anatomical shape, and the transformation functions ϕ^i, which maps every i^{th} patient-specific form [58]. Then each shape was describable as the sum of the model $\bar{T}$ and some residual ϵ^i (figure 2.2):

$$T^i = \phi^i \bar{T} + \epsilon^i \tag{2.3}$$

The function ϕ^i was explain using the LDDMM method [56], and it was parameterized by a time-varying velocity field only identifies by an initial vector speed v_0^i:

$$v_0^i(x) = \sum_k K_v(x_k, x)\beta_{x_k}^i \tag{2.4}$$

Deformetrica takes as input the femur shapes and kernel widths (λ_W and λ_V), while outputting the template shape, the reconstructed input forms, the control point coordinates and relative moment vectors.

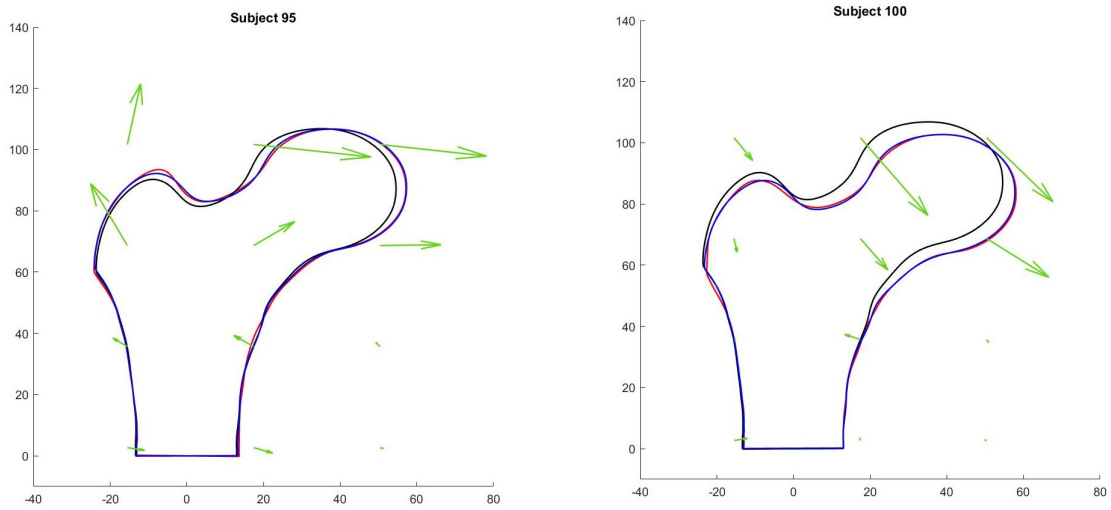

Figure 2.2: *Example of how the template was deform to derive a random external profile. The red line identifies the original external boundary, the black one identifies the template boundary and the blue line identifies the contour obtained by applying the moments to the template*

2.4 Sensitivity Analysis

The Sensitivity Analysis (SA) allows to evaluate different parameters and determine which are the influencing factors and not influential. Thus, the values of the input factors of the model are perturbed (individually, in groups or at the same time) within a fixed range of variation in order to identify the sensitivity for each factor of the model [59, 60]. In this thesis, sensitivity analysis has been used to derive the input parameters of Deformetrica that allow us to obtain a more accurate reconstruction of femur external profile. The parameters studied are described below [49, 55, 61, 62].

- **Optimization method**: Each Deformetrica model use those deformation and attachment mechanics to define a specific cost function, that will then be optimized either by steepest gradient descent (*GradientAscent*) or with the limited-memory Broyden-Fletcher-Goldfarb-Shanno (L-BFGS) method (*ScipyLBFG*).
  Both methods are used to minimize the function, for the GradientAscent the minimization is performed following the maximum descent determined by the opposite of the gradient of a point; while ScipyLBFG method uses the derivatives of the function to identify the steepest descent from which to derive the Hessian matrix that will guide the minimization.
  A further difference is that in certain situations the Gradient method is more robust than the Scipy one, which however converges more quickly and has limited memory consumption.

- **Kernel type**: The deformation mechanics heavily rely on convolution operations, *Keops* uses linear convolutions for calculating 2D array reductions, while *Torch* uses quadratic convolutions.
  The main difference is in the computation speed and memory used. In addition, it is advisable to use the Keops kernel when there are many points, to avoid that during a simulation deformation goes out of memory.

- **Kernel width**: The Kernel width is a numeric value that defines the size of the kernel used. There are two kernels: λ_W defines the *resolution* of the deformetric output, value that are too small tend to make the shape orthogonal, while too large values tend to make all shape alike and therefore alter matching accuracy, and λ_V defines the *stiffness* of the deformation, so increasing this parameter increases the stiffness of the deformation, with smaller values the model consider more independent local variations and the information in larger anatomical regions is not well integrated, while with larger values the model is based on almost rigid deformations.
  The sensitivity analysis of these parameters is performed following the article of Bruse and collaborators [63], which consisted in running Deformetrica many times altering λ_W and λ_V values in order to achieve an optimal reconstruction of the input shapes. Two starting values for λ_W and λ_V were calculated as a percentage of the femur that had the shortest area. Thus, a starting template was calculated from these values and each i^{th} patient-specific shape was reconstructed from the output transformation function. Then, λ_W and λ_V were decreased with a 1 mm step and the reconstruction error (Eq. 2.5) was calculated.

$$\epsilon_s = \sqrt{\frac{1}{N}\sum_{i=1}^{N} ||x_i^s - x_i^r||^2} \tag{2.5}$$

  where N is the number of point, x_i^s is the i^{th} node of the original profile and x_i^r is the i^{th} node of the reconstructed profile.
  This step was performed until the reconstruction error was reduced by $\geq 80\%$.

- **Attchment type**: The attachment-type is the type of distance used between objects, it depends on the size of the Gaussian kernel (λ_W) and allows to assess whether the reconstruction is close to the original.
  There are three parameters to edit: *Varifold*, *Current* and *Landmark*. The main difference between these parameters is the calculation of the distance between two meshes and the orientation of the normal. Varifold does not take into account the orientation as opposed to current; while the Landmark parameter requires a correspondence between points, in this case there was no correlation between points so this method was discarded.

- **Noise-std**: Finally, Noise-std parameter controls the adaptability of the reconstructed profile to the original ones, it only controls the compromise between data attachment and regularization.

In addition, with the aim of assessing whether the final form of the template had not been heavily modified by one shape, which was included or discarded, an outlier search has been carried out following the article by Bruse and collaborators [63], in which they performs k-fold cross-validation. The entire dataset was split into k=50 random subsets: thus, the template was calculated k times, each time discarding a different subset (consisting of 2 subjects) until all subjects were discarded once. 50 different templates were obtained and the distances between them were calculated, in particular considering the larger distance values, the medium ones and the Hausdorff distance. From the obtained values, shown in the figure 2.3, the highest value was $0.6076mm$, $0.2733mm$ and $0.6076mm$ for the largest, the average and Hausdorff distance respectively, which were evaluated satisfactory to say that no shape did affect the template building.

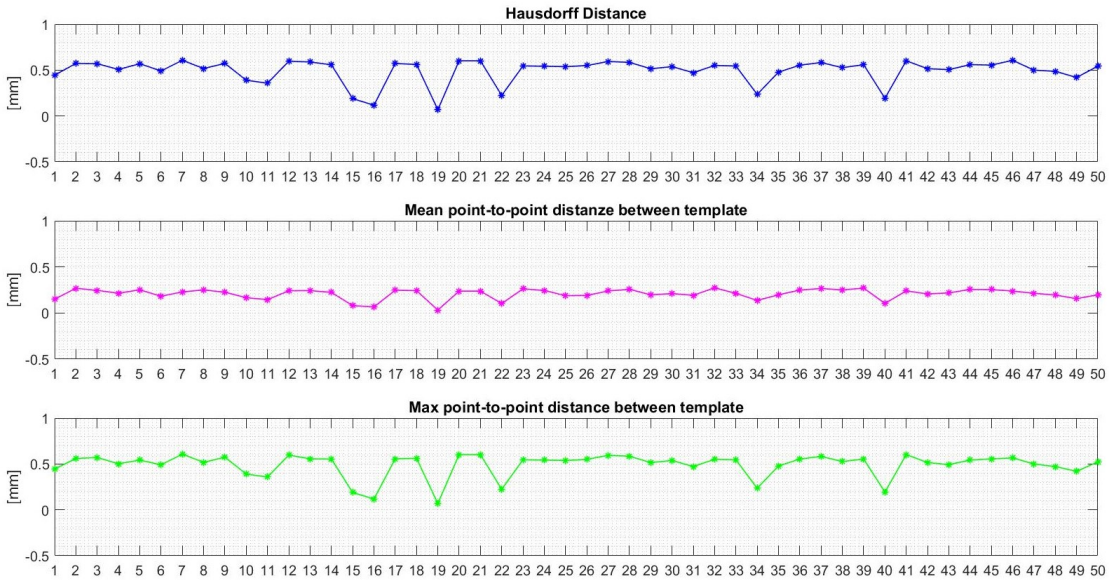

Figure 2.3: *Obtained value of the largest, average and Hausdorff distance to estimate that no subject affects the template construction.*

2.5 Statistical Shape Model

Statistical Shape Models (SSM) are geometric models that represent a collection of matching objects in a very compact way. In general, SSMs denote an average shape of many objects as well as their variation in shape [18, 64]. The SSMs were created using the Nx2k moment vectors matrix X_β as input, with N being the total number of patients and k dependent on the number of control points.
Herein, two separate methods were utilized to create SSMs: PCA and PLS. While PCA maximized the variance found in the femurs anatomical features, PLS identified the modes maximizing the covariance between femurs anatomical features and the patient-specific fracture status, which was known. By projecting the original data matrix on the recognize modes, the PCA (b_i) and PLS (t_i) shape components for each i^{th} mode ($i = 1, ..., N-1$) could be computed [18].
A schematic of the workflow is presented in Figure 2.4.

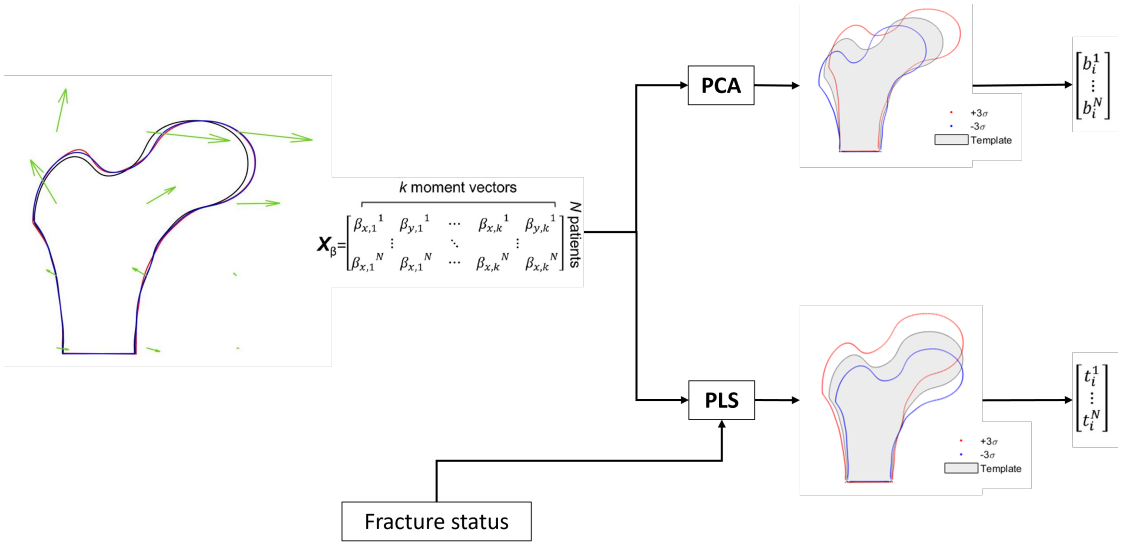

Figure 2.4: *Statistical Shape Analysis pipeline, where X_β was the moment vectors matrix, while b_i and t_i were the shape components for each i^{th} mode.*

2.5.1 Principal Component Analysis

PCA is a statistical approach that allows extracting the main shape features observable in an input population. Basically, it is based on the idea [65] of decreasing the dimensionality of a dataset by going to preserve as much "variability" as possible (i.e. statistical information, $max_{|q|=1} var(Xq)$ where q being the searched basis and X the input variable). It performs this reduction by identifying the directions, called modes, along which the variation in the data is maximum [66]. In essence, it is reduced to the resolution of an eigenvalue problem ($Sq = \lambda q$), in which the *eigenvectors* (q), represent the main modes of variation, that is, the orthogonal paths along which the variance is maximized, and *eigenvalues* (λ), indicate the fragment of the total variance reported by each mode [4].

After recognizing the modes, that maximize the variance of the initial variables, the components are found projecting the initial variables on the modes [18, 67]. Here, each component reveals the mode's contribution to the specific femur shape of the subject. The modes taken into consideration will be those defined as more influential, i.e. that explain a specific $\pi\%$ of the entire variance, discarding the others and thus producing a minimized representation of the original dataset.
Having only the information on the proximal shape of the femur of our population, produced by Defometrica, the PCA was applied on the shape.

PCA-based Statistical Shape Model: A PCA-based Statistical Shape Model was created upon patient-specific moment vectors β (a Deformetrica's output), containing the proximal femur anatomical details of the i^{th} subject referred to the template [4, 18]. The starting point of the SSMs construction, was the building of a moment vectors matrix ($X_\beta = [\tilde{\beta^1}; ...; \tilde{\beta^N}]$, where $\tilde{\beta^i} = \beta^i - \bar{\beta}$ the centered moment vectors), on which PCA was performed. Subsequently, from this matrix was obtained the covariance matrix (Eq. 2.6).

$$S = \frac{1}{N-1} \sum_{i=1}^{N} (x_i - \bar{x})(x_i - \bar{x})^T \tag{2.6}$$

where N is the number of subjects, x_i the i^{th} moment and $\bar{x} = \frac{1}{N} \sum_{i=1}^{N} x_i$.
PCA was conducted to determine the principal geometrical attributes observed in the cohort and allowed the extraction of the deformation modes concurrently with their respective variance and related shape principal components; so principal components describe the deformation that the template experiences along the i^{th} direction to correspond each subject's shape [4, 18]. The principal components give therefore a quantitative illustration of the subject-specific shape attributes contained in each mode [18].
To see the effect of each m^{th} specific deformation mode on the template, the equivalent set of moment vector β^m, parametrizing the related template transformation only along the m^{th} mode can be determined.

$$\beta^m = \bar{\beta} \pm l\sqrt{\lambda_m} q_m \tag{2.7}$$

Substituting β^m of Equation 2.7 in Equation 2.4, is possible to determine the initial velocity used to deform the template along the mode of interest [4].

2.5.2 Partial Least Square

However, PCA alone is able to extract only the directions (or modes) of greater variability, without taking into account an external variable of interest [4]; for this reason, PLS is generally used, taking a matrix of predictors and a matrix of response variables in input, identify the main characteristics of the predictor matrix that are also relevant for the response variable.
This method identifies new bases, also relevant to an external response variable, within the predictor space; then it calculates the space that maximizes the covariance between the X_c predictor matrix and an array of Y_c response variables. Mathematically, PLS calculates the weights vectors r and s which fulfill:

$$max_{|r||s|=1} cov(X_c r, Y_c s) = max_{|r||s|=1} var(X_c r) corr(X_c r, Y_c s)^2 var(Y_c s) \tag{2.8}$$

as the contrary of PCA, which solves $max_{|r|=1} var(X_c r)$.
The algorithm follows an iterative process, summarize in figure 2.5. This loops stop when all PLS modes are extracted; furthermore, at each step, the variance explained by r and s is removed.

Inputs: $\mathbf{X}_C$, $\mathbf{Y}_C$, number of PLS modes p to extract ($p = N - 1$)

for $n = 1$ to p **do**

$\boldsymbol{r}^n \leftarrow first\ eigenvector\ of\ \mathbf{X}_C^{n\,T}\mathbf{Y}_C^n\mathbf{Y}_C^{n\,T}\mathbf{X}_C^n\ (from\ [145])$

$\mathbf{t}^n \leftarrow \mathbf{X}_C^n\boldsymbol{r}^n/|\boldsymbol{r}^n| \quad n^{th}\ PLS\ component\ of\ \mathbf{X}_C$

$\mathbf{s}^n \leftarrow \mathbf{Y}_C^n\boldsymbol{t}^n/(t^{n\,T}t^n)$

$\mathbf{u}^n \leftarrow \mathbf{Y}_C^n\boldsymbol{s}^n/|\boldsymbol{s}^n| \quad n^{th}\ PLS\ component\ of\ \mathbf{Y}_C$

$\mathbf{p}^n \leftarrow \mathbf{X}_C^n\boldsymbol{t}^n/(\boldsymbol{t}^{n\,T}\boldsymbol{t}^n) \quad n^{th}\ PLS\ loading\ of\ \mathbf{X}_C$

$\mathbf{q}^n \leftarrow \mathbf{Y}_C^n\boldsymbol{u}^n/(\boldsymbol{u}^{n\,T}\boldsymbol{u}^n) \quad n^{th}\ PLS\ loading\ of\ \mathbf{Y}_C$

$\mathbf{X}_C^{n+1} \leftarrow \mathbf{X}_C^n - \boldsymbol{t}^n\boldsymbol{p}^{n\,T} \quad deflation\ of\ \mathbf{X}_C$

$\mathbf{Y}_C^{n+1} \leftarrow \mathbf{Y}_C^n - \boldsymbol{t}^n[\boldsymbol{t}^{n\,T}\mathbf{Y}_C^n/(\boldsymbol{t}^{n\,T}\boldsymbol{t}^n)] \quad deflation\ of\ \mathbf{Y}_C$

end

Figure 2.5: *PLS space decomposition (PLS1 algorithm)*

The goal was the extraction of the dominant shape features considerable correlated to the risk of proximal femur fracture [4].

PLS-based Statistical Shape Model: A PLS-based Statistical Shape Model has the aim to study the main shape features most relevant to the risk of fracture. Here, PLS was applied to the moment vectors matrix X_β, taking the centered fracture status vectors as the response variable. With the PLS1 algorithm, the shape modes were identified automatically ordered by reducing variance and covariance for the response variable[4, 18]. Therefore, the first c PLS components were selected, explaining contemporary $\pi_{X\beta}\%$ of the variance in X_β and $\pi_{FS}\%$ of the total fracture status variance.
The visualization of the n^{th} PLS deformation mode is achieved warping the template using the moment vectors determined as:

$$\beta^n = \bar{\beta} \pm l\sqrt{\lambda_n}p_n \tag{2.9}$$

Finally, like PCA-based SSM, substituting the Equation 2.9 in Equation 2.4, the initial velocity to be used to deform the template along the mode of interest can be chosen[4].

2.6 Prediction of fracture risk

The identified, PCA and PLS, modes were used for the implementation of logistic regression models for the prediction of the patients' fracture status, which were tested using a 10-fold cross-validation procedure [68].

More in detail, the first two, three, four and five PCA and PLS components of SSM were considered here as separate predictors, leading to eight distinct predictive models (four for PCA and four for PLS). The prediction ability of these logistic regression models was compared with that of a different regression model using aBMD as an independent variable and the fractured status as a binary dependent variable. A test set would be required for the predictive performance of the method to be assessed, a k-fold cross-validation technique was adopted according to the steps shown in the following figure 2.6 [68].

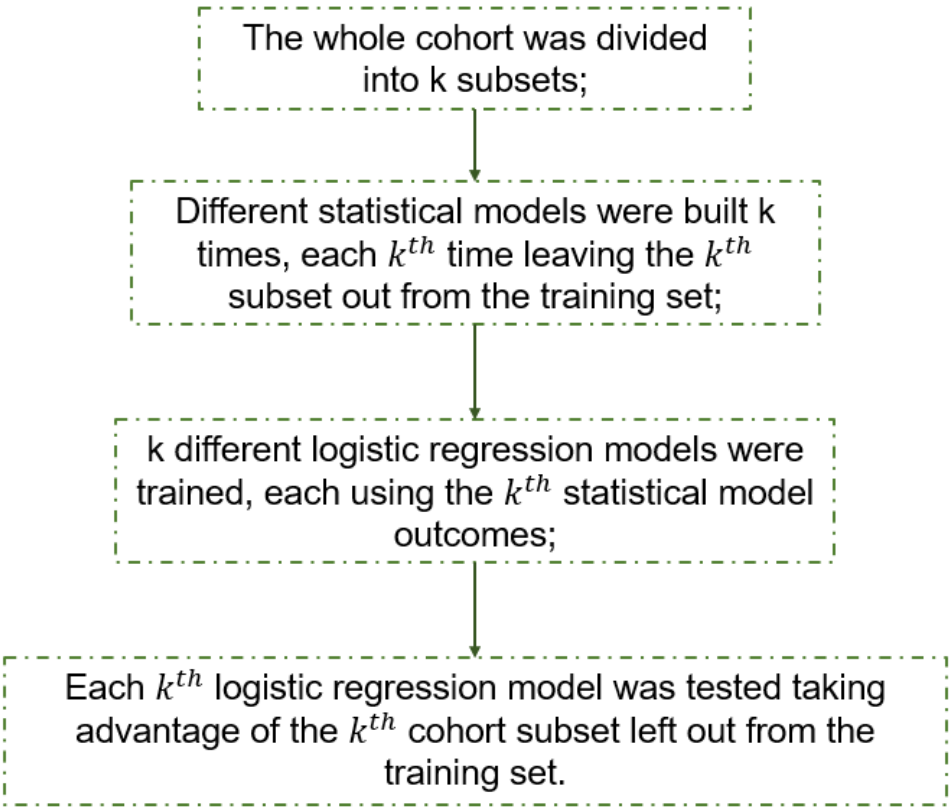

Figure 2.6: *k-fold cross-validation step*

Particularly, here was applied a 10-fold cross-validation. The whole cohort was separated into 10 groups in a random way and each group was forced, as far as possible, to have the same number of fractured subjects and controls one, to ensure training sets are properly balanced [68].

PCA and PLS were executed and the logistic regression models were trained and tested 10 separate times, predicting the fracture risk for the subjects contained in the test group. Then, the respective Receiver Operating Characteristic (ROC) curves were plotted and the Area Under Curve (AUC) was calculated for each ROC curve, with the aim to compare the value of the different logistic regression models.

3. Results

3.1 Sensitivity Analysis

The sensitivity analysis was executed to examine the effect of different parameters on the Deformatrica's output in order to derive the optimal inputs to obtain an accurate reconstruction of the external profile of the femur. The results of this analysis are described below.

- **Optimization method**: Deformetrica runs two times, one with the GradientAscent method and the other with the ScipyLBFGS method. In Table 3.1 and the graph in figure 3.1 the differences between the two methods are shown, so is possible to say that the ScipyLBFGS method shows a better reconstruction than GradientAscent one, because it has smaller residuals and Hausdorff distances. Aiming to evaluate if the two methods modify the Deformetrica's template output, the Hausdorff distance between them was computed, obtaining a value of $0.768mm$.

Table 3.1: *Comparison between GradientAscent optimization method and ScipyLBFGS optimization method*

$\lambda_W = 15$ $\lambda_V = 20$	**GradientAscent**	**ScipyLBFGS**	**Percentage difference**
Residual comparison	Max=100.057 Mean=25.867 Min=3.318	Max=92.584 Mean=24.445 Min=2.816	Max=7.47% Mean=5.50% Min=15.13%
Hausdorff distance comparison	Max=4.344 Mean=2.107 Min=1.015	Max=4.064 Mean=2.008 Min=0.892	Max=6.45% Mean=4.72% Min=12.06%

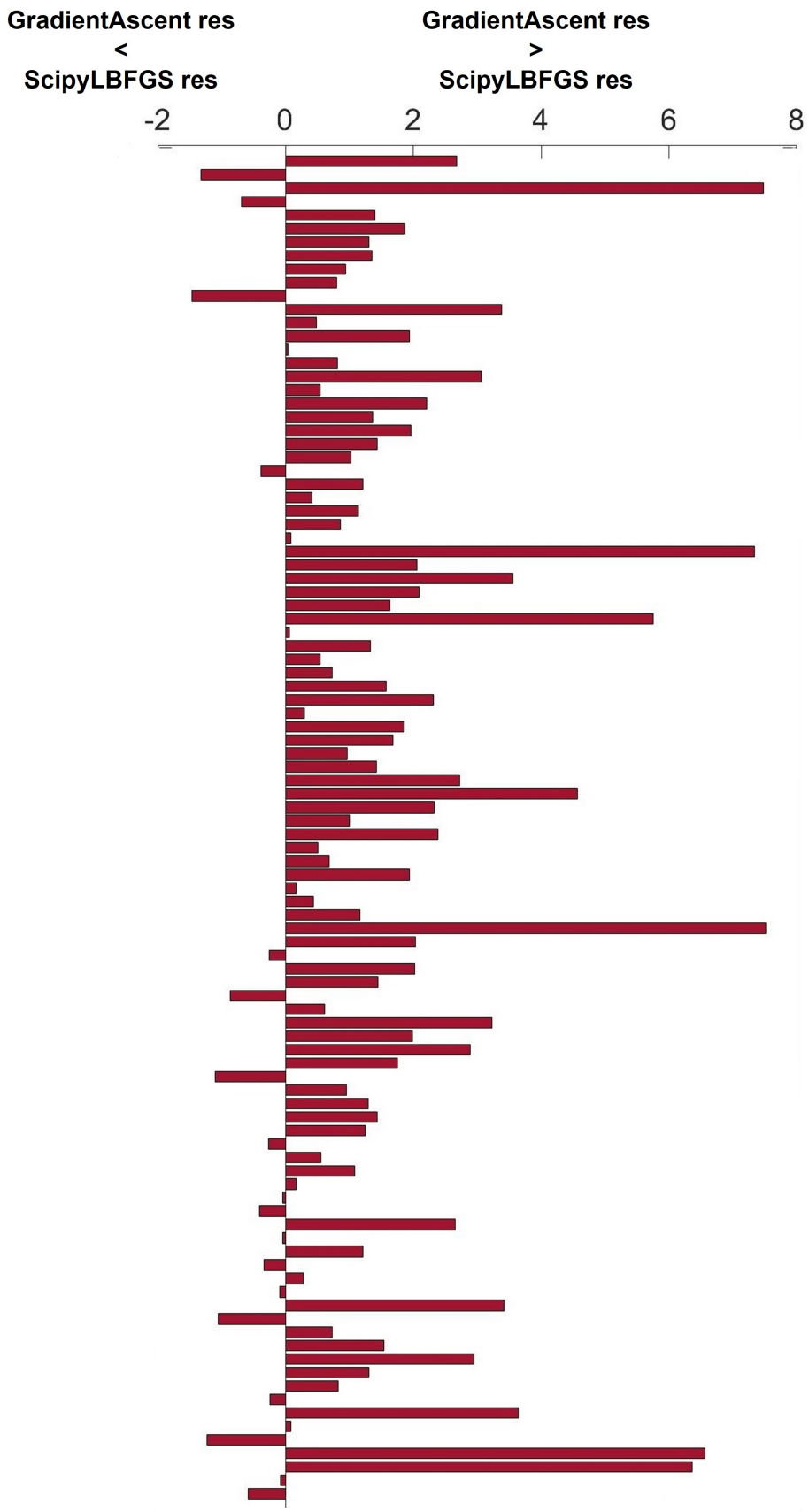

Figure 3.1: *Difference between the residual of GradientAscent method and ScipyLBFGS method. Each bar corresponds to a subject, the positive bars identify how much the GradientAscent residue is greater than the ScipyLBFGS.*

- **Kernel type**: Also in this case the kernel type used did not affect the construction of the template, the Hausdorff distance obtained is $0.054mm$. The percentage differences observed in table 3.2 and the comparison of residues (fig. 3.2), allow to say that the kernel Torch has a greater influence on the reconstruction of the femoral profiles.

Table 3.2: *Comparison between Keops and torch kernel type*

$\lambda_W = 15$ $\lambda_V = 20$	**Keops**	**Torch**	**Percentage difference**
Residual comparison	Max=92.584 Mean=24.445 Min=2.816	Max=89.393 Mean=23.907 Min=2.787	Max=3.45% Mean=2.20% Min=1.04%
Hausdorff distance comparison	Max=4.064 Mean=2.008 Min=0.892	Max=4.019 Mean=1.999 Min=0.900	Max=1.11% Mean=0.46% Min=-0.79%

- **Kernel width**: Two starting values for λ_W and λ_V were calculated as a percentage of the smallest proximal femur area (Eq. 3.1) [63], which generated an initial λ_W of 30mm and a λ_V of 40mm.

$$\begin{aligned} \lambda_W &= \sqrt{pw\% * A_{min}} \\ \lambda_V &= \sqrt{pv\% * A_{min}} \end{aligned} \tag{3.1}$$

  Where A_{min} is the shortest proximal femur area (subject 30), while $pw\%$ and $pv\%$ was chosen equal to 20% and 40% respectively. Therefore, an initial template was calculated from those values and each i^{th} patient-specific shape was reconstructed. Then, the two kernels were gradually changed while evaluating the overall reconstruction error (RMSE), which was calculated by comparing the input shapes with the reconstructed ones. Eventually, this procedure produced the optimal λ_W and λ_V values of 15 and 33 mm respectively. Table 3.3 shows the used λ_W and λ_V values, with the corresponding RMS errors of the smallest subject.

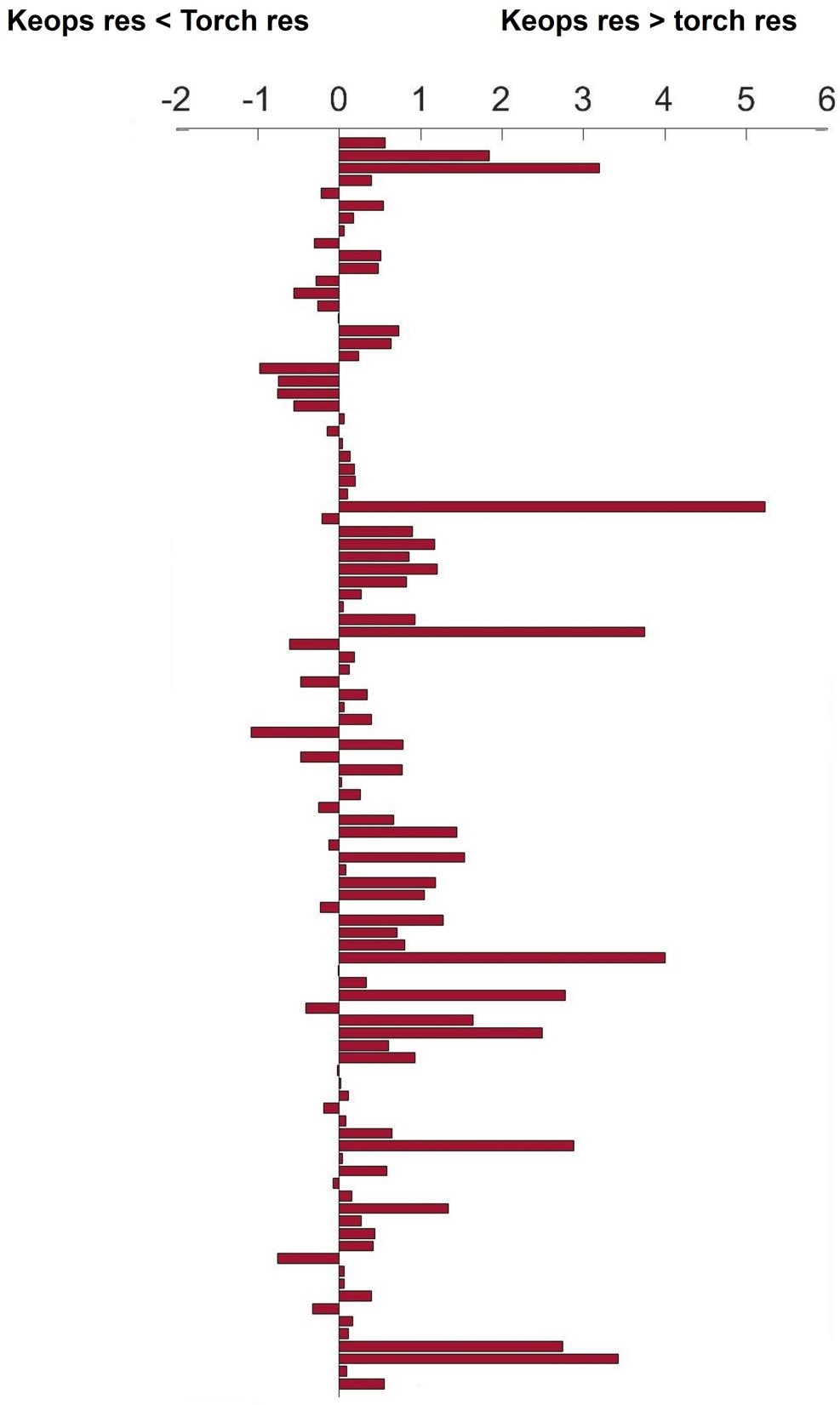

Figure 3.2: *Difference between the residual of Keops and Torch method. Each bar corresponds to a subject, the positive bars identify how much the Keops residue is greater than the Torch.*

Table 3.3: *RMSE corresponding to the different λ_W,λ_v pairs explorer. The colored cell is the pairs used.*

λ_W (mm)	λ_V (mm)	**RMSE**	λ_W (mm)	λ_V (mm)	**RMSE**	λ_W (mm)	λ_V (mm)	**RMSE**	λ_W (mm)	λ_V (mm)	**RMSE**	λ_W (mm)	λ_V (mm)	**RMSE**
30	40	4.2069	27	31	1.6702	23	33	1.1811	20	32	1.1513	17	36	1.0621
30	39	4.1732	27	30	1.6987	23	32	1.2958	20	31	1.0710	17	35	1.0736
30	38	4.1768	26	40	4.1999	23	31	1.3608	20	30	1.1686	17	34	0.9082
30	37	4.1812	26	39	4.1659	23	30	1.4259	20	29	1.1722	17	33	0.9714
30	36	1.6897	26	38	4.1693	22	40	1.2361	20	28	1.2403	17	32	0.8918
30	35	1.5592	26	37	4.1737	22	39	1.1039	20	27	1.2895	17	31	1.0635
30	34	1.5038	26	36	1.4897	22	38	1.0738	20	26	1.0863	17	30	1.0649
30	33	1.7809	26	35	1.4184	22	37	1.1681	20	25	1.1706	17	29	1.0892
30	32	1.9273	26	34	1.1886	22	36	1.1821	19	40	1.1698	17	28	0.9736
30	31	1.8249	26	33	1.4455	22	35	1.1171	19	39	1.0818	17	27	1.1461
30	30	1.8876	26	32	1.2850	22	34	1.1167	19	38	1.1459	17	26	1.0304
30	29	1.9485	26	31	1.5003	22	33	1.1458	19	37	1.1391	17	25	1.0309
30	28	1.9958	26	30	1.2808	22	32	1.1871	19	36	1.1382	16	40	1.1528
29	40	4.2037	26	29	1.6409	22	31	1.2223	19	35	1.1395	16	39	1.0458
29	39	4.1699	25	40	4.2002	22	30	1.2385	19	34	1.0166	16	38	0.9902
29	38	4.1734	25	39	4.1658	22	29	1.2762	19	33	1.0783	16	37	1.0577
29	37	4.1776	25	38	4.1693	22	28	1.2963	19	32	1.0857	16	36	1.0568
29	36	1.5844	25	37	1.3373	22	27	1.3887	19	31	0.9925	16	35	1.1250
29	35	1.5087	25	36	1.1488	22	26	1.2694	19	30	1.0499	16	34	0.9048
29	34	1.7120	25	35	1.4245	22	25	1.3809	19	29	1.0862	16	33	0.9224
29	33	1.4549	25	34	1.3046	21	40	1.2184	19	28	1.1886	16	32	1.0334
29	32	1.6961	25	33	1.3408	21	39	1.1649	19	27	1.3232	16	31	0.9376
29	31	1.7308	25	32	1.3954	21	38	1.0049	19	26	1.1116	16	30	1.1008
29	30	1.7387	25	31	3.4197	21	37	1.1910	19	25	1.2025	16	29	1.0476
28	40	4.2016	25	30	1.5387	21	36	1.2337	18	40	1.2446	16	28	1.8623
28	39	4.1679	25	29	1.5039	21	35	1.2864	18	39	1.1715	16	27	1.0839
28	38	4.1711	24	40	4.2011	21	34	0.9472	18	38	0.9962	16	26	1.0136
28	37	4.1753	24	39	1.2161	21	33	1.1726	18	37	0.9863	16	25	1.0714
28	36	1.3556	24	38	1.2610	21	32	1.0967	18	36	1.0965	15	40	1.1859
28	35	1.3383	24	37	1.3202	21	31	1.0995	18	35	1.1636	15	39	0.9588
28	34	1.3186	24	36	1.2673	21	30	1.1027	18	34	1.0715	15	38	0.9709
28	33	1.4130	24	35	1.3636	21	29	1.2134	18	33	1.0265	15	37	1.0328
28	32	1.6691	24	34	1.4172	21	28	1.2440	18	32	0.9937	15	36	1.0285
28	31	1.3508	24	33	1.2834	21	27	1.3078	18	31	1.0705	15	35	1.1607
28	30	1.6917	24	32	1.4505	21	26	1.1942	18	30	0.9715	15	34	0.9240
27	40	4.2003	24	31	1.2905	21	25	1.2459	18	29	1.0726	15	33	0.8520
27	39	4.1667	24	30	1.4705	20	40	1.2304	18	28	1.1162	15	32	0.8865
27	38	4.1700	23	40	1.3338	20	39	1.2058	18	27	1.0804	15	31	0.9747
27	37	4.1743	23	39	1.2016	20	38	1.3792	18	26	1.0544	15	30	0.9612
27	36	1.3647	23	38	1.1093	20	37	1.0407	18	25	1.0387	15	29	1.0597
27	35	1.4453	23	37	1.4503	20	36	1.1212	17	40	1.9283	15	28	1.0618
27	34	1.2777	23	36	1.1453	20	35	1.1673	17	39	1.0488	15	27	1.0486
27	33	1.5157	23	35	1.2954	20	34	1.1189	17	38	1.0668	15	26	1.8212
27	32	1.4979	23	34	1.2963	20	33	1.1693	17	37	1.0406	15	25	1.0424

- **Attachment type**: Deformetrica run with the Current attachment type and with Varifold, the landmark one was discarded because we did not have a correspondence between points. Current attachment was the best one according to figure 3.3 and table 3.4; while the template Hausdorff distance was $0.909mm$.

Table 3.4: *Comparison between Current and Varifold attachment type*

$\lambda_W = 15$ $\lambda_V = 33$	**Current**	**Varifold**	**Percentage difference**
Residual comparison	Max=110.411 Mean=35.801 Min=8.141	Max=149.580 Mean=41.716 Min=10.330	Max=-35.48% Mean=-16.52% Min=-26.90%
Hausdorff distance comparison	Max=3.885 Mean=2.251 Min=1.131	Max=4.293 Mean=1.949 Min=1.040	Max=-10.50% Mean=13.40% Min=8.05%

- **Noise-std**: With a visual inspection of the table 3.5 a noise value equal to 0.1 was choose, which have the lowest residual and Hausdorff distance, also visible in figure 3.4.

Table 3.5: *Comparison between four noise-std*

$\lambda_W = 15$ $\lambda_V = 33$	**Noise-std=0.01**	**Noise-std=0.1**	**Noise-std=1**	**Noise-std=10**
Residual comparison	Max=88.357 Mean=26.598 Min=4.472	Max=88.288 Mean=26.565 Min=4.497	Max=110.411 Mean=35.801 Min=8.141	Max=2472.773 Mean=688.95 Min=63.928
Hausdorff distance comparison	Max=3.982 Mean=2.064 Min=1.062	Max=3.977 Mean=2.061 Min=1.064	Max=3.835 Mean=2.222 Min=1.184	Max=13.228 Mean=6.936 Min=2.399

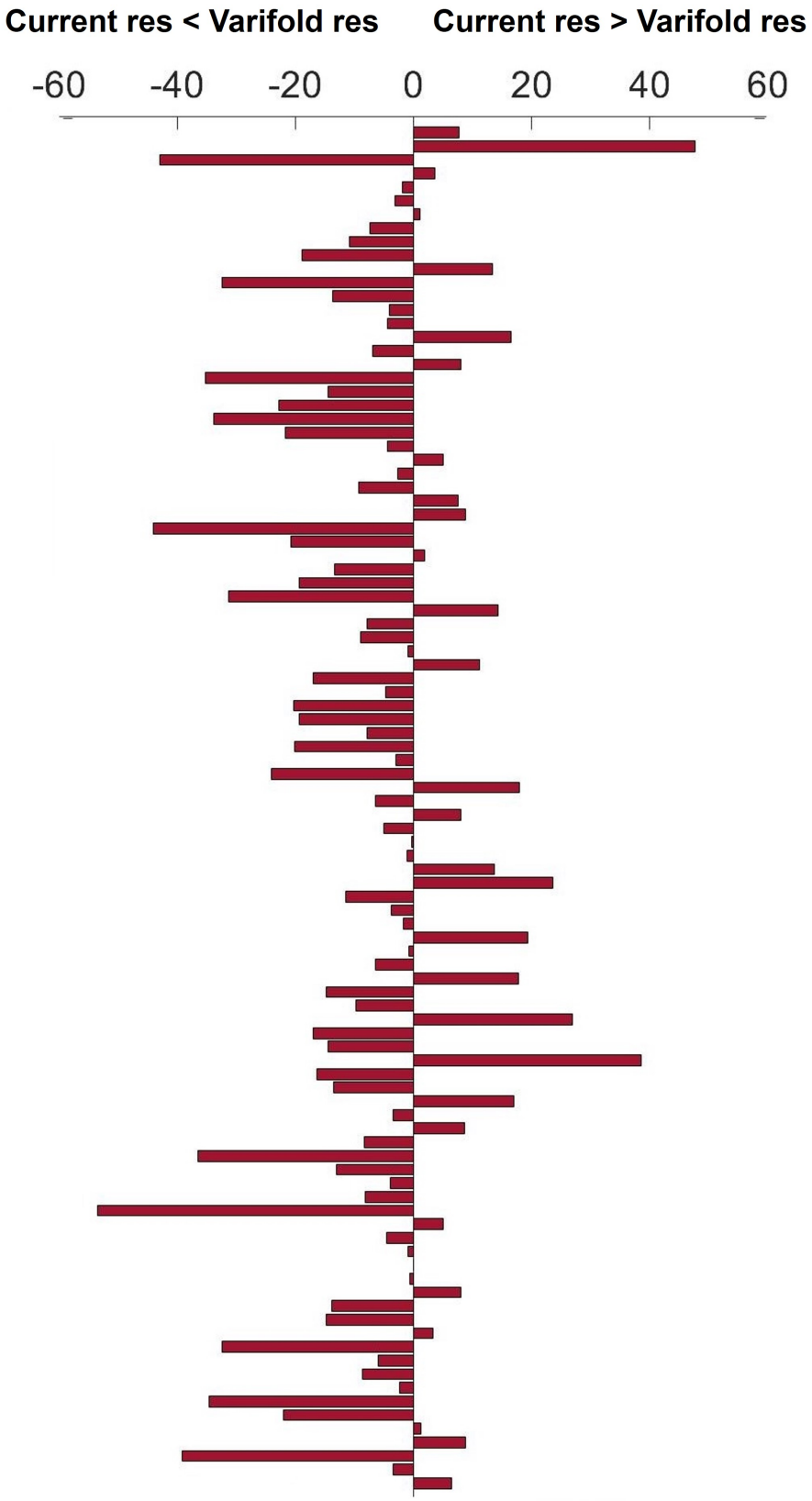

Figure 3.3: *Difference between the residual of Current and Varifold method. Each bar corresponds to a subject, the positive bars identify how much the Current residues is greater than the Varifold.*

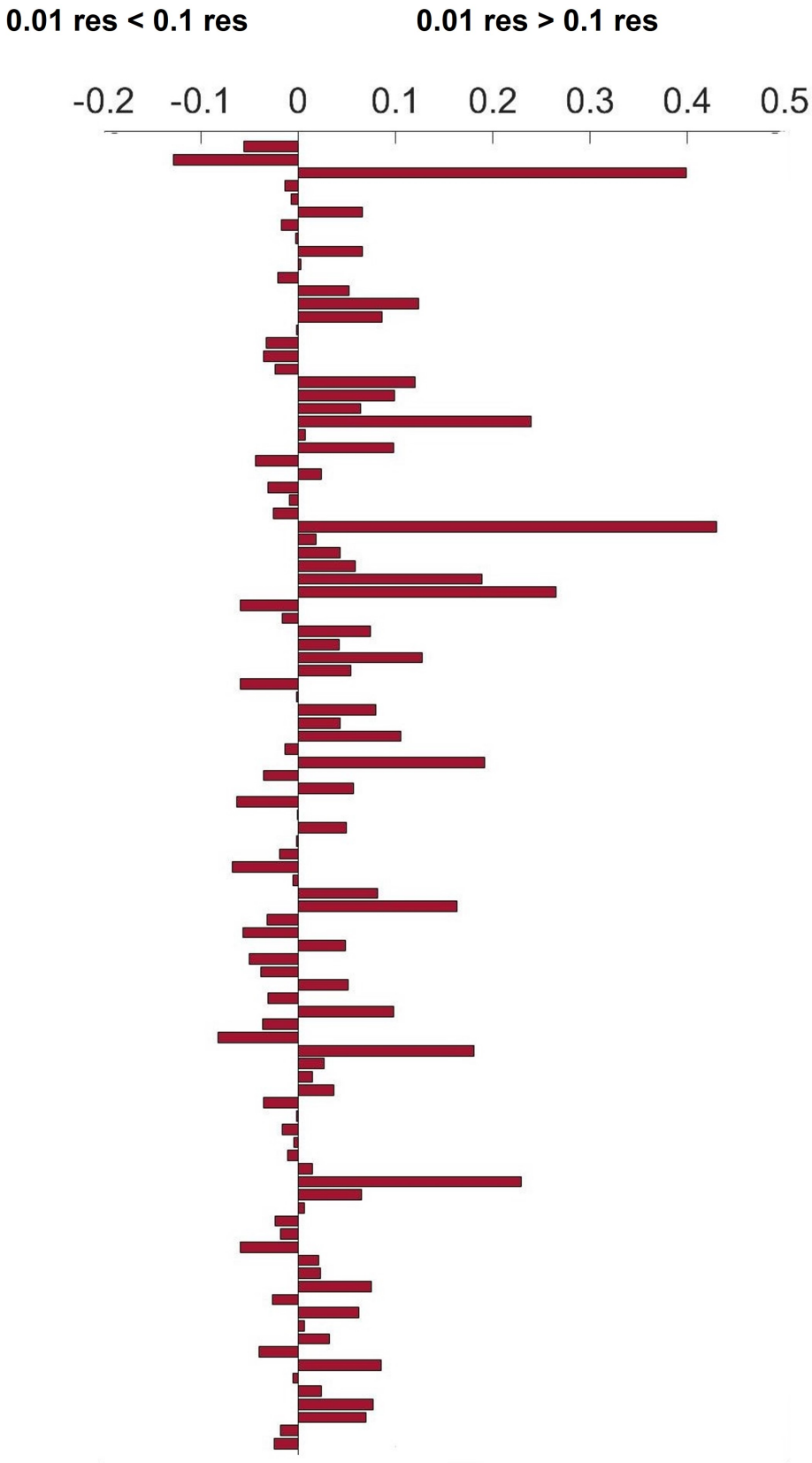

Figure 3.4: *Difference between the residual of noise-std equal to 0.01 and 0.1. Each bar corresponds to a subject, the positive bars identify how much the noise-std equal to 0.01 residues is greater than the 0.1 residues.*

3.2 Statistical Shape Model

Deformetrica was run once more using the combination of input parameters as obtained by the previously presented sensitivity analysis. The outputs obtained (template, control point coordinates and patient-specific moments) were used for the creation of the statistical model based on the shape.
Using λ_V equal to 33, 24 vectors moment (x,y pairs) per patient were obtained. So the moment matrix X_β had a size of 96X24.

PCA: The first method performed is PCA conducted on the X_β matrix (96X24). The first 5 PCA modes were assigned, able to explain 96.54% of the total shape variance (Figure 3.5(a)).

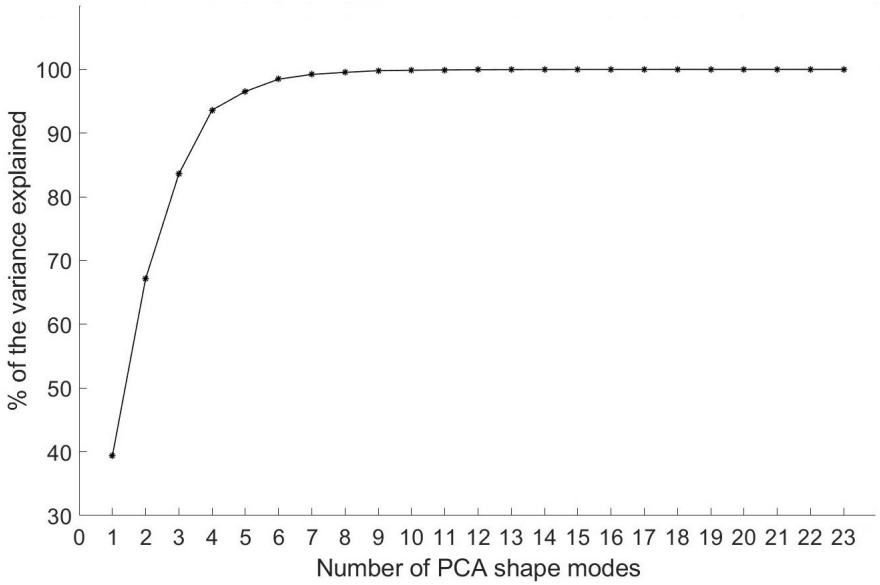

(a)

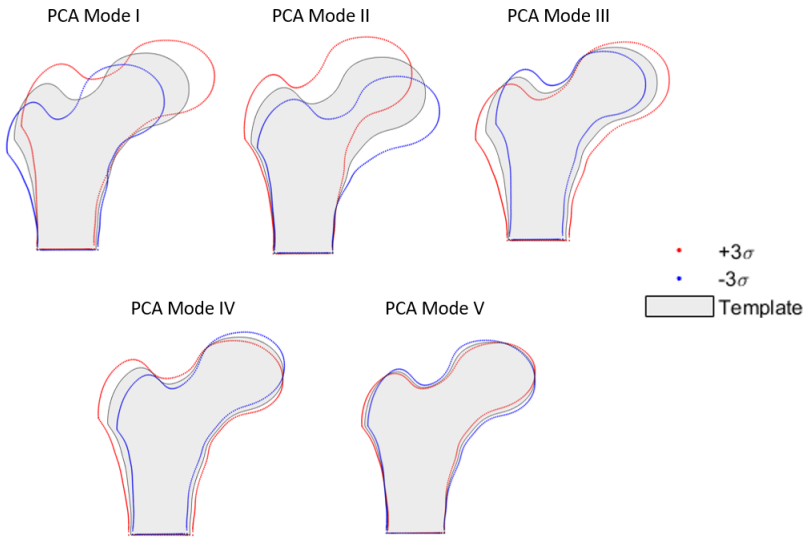

(b)

Figure 3.5: *(a) Cumulative percentage of variance described by the PCA shape modes. The first 5 components demonstrated 96% of the total variance shape and the first three modes explained 83% of the total variance shape. (b) Representation of the first 5 PCA deformation modes.*

The selected modes can be visualized in the figure 3.5(b), in which the deviations of $\pm c\sqrt{\lambda}$, with $c = 3$, were shown. By a first visual inspection, size, inclination and length of the neck represent the main shape features. It is also possible to observe a correlation between the different modes and the HSA parameters (Fig. 3.6) obtained in a previous 3D study [68]. In particular mode 1 and 3 was correlated with Hip Axial Length (HAL) (mode 1: $R = 0.27$, $p = 0.0085$, mode 3: $R = 0.34$, $p = 0.00069$); while mode 1 and 2 with NSA (mode 1: $R = -0.43$, $p = 0.0000076$, mode 2: $R = 0.43$, $p = 0.000014$); this suggests that HAL and NSA are highly variable features. It is interesting to observe that all modes do not have a correlation with aBMD, which suggests that the only use of shape is not sufficient to assess fracture risk.

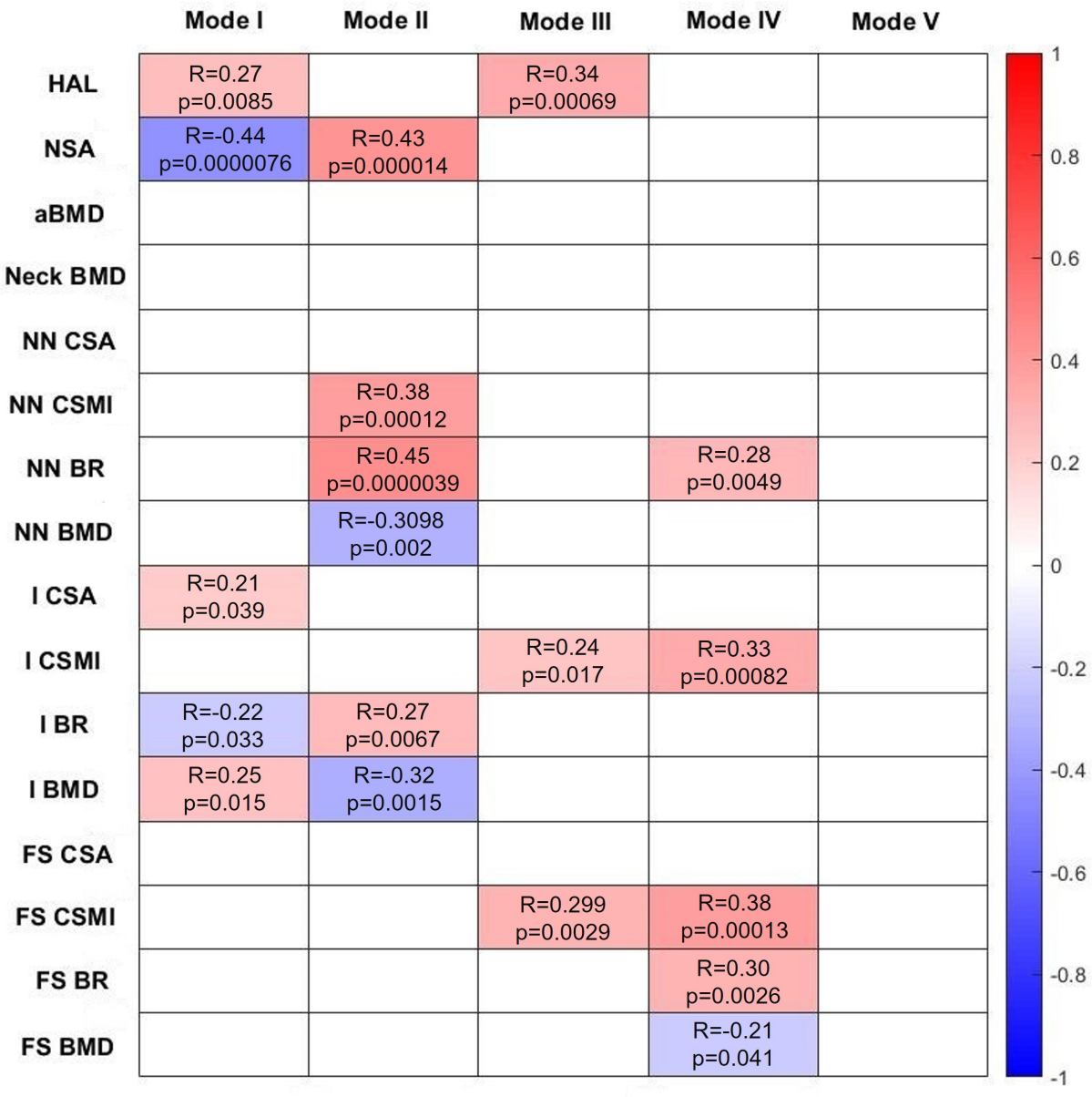

Figure 3.6: *Correlation Matrix Plot of PCA mode and HSA parameters*

PLS: A total of 5 PLS modes managed to describe 95.14% of the shape variance (figure 3.7(a)). In this case, only one outward variable was included within PLS, the PLS modes were ordered with the condition to have reducing variance in the shape as well as reducing covariance between shape and FS. The irregular decrease in the disclosed shape and FS variability by the PLS shape modes, therefore, appears to support a limited function of the femur shape in describing the variations observed in the FS.

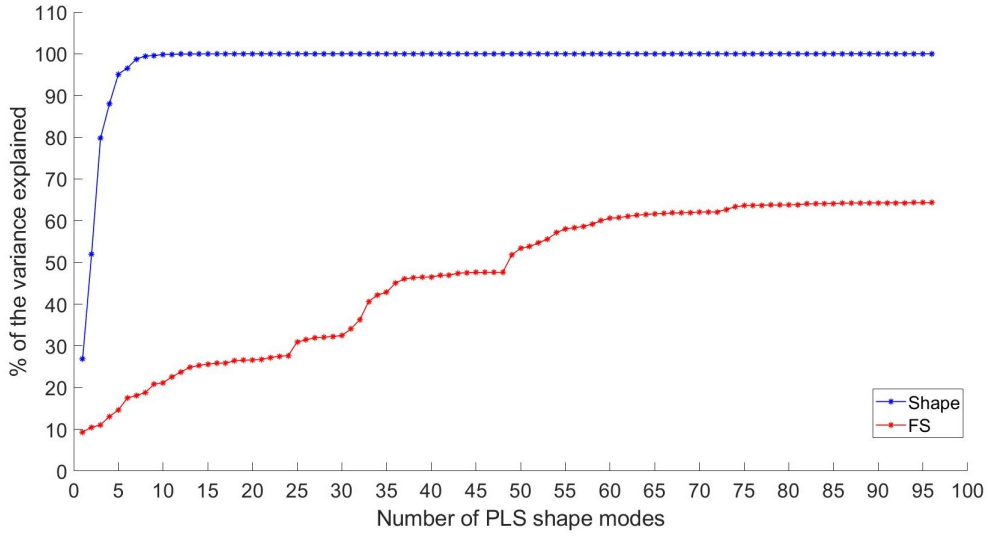

(a)

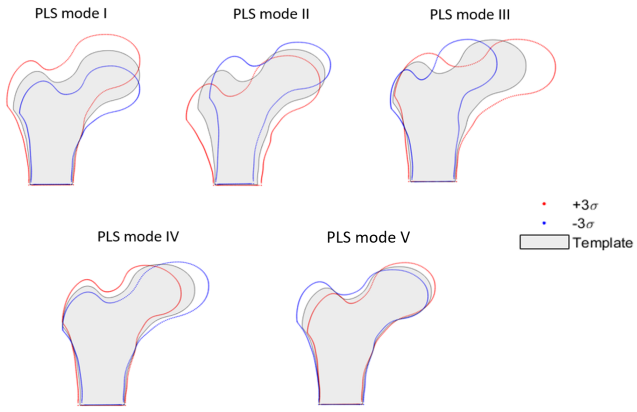

(b)

Figure 3.7: *(a) Cumulative percentage of variance described by the PLS shape modes. The first 5 components demonstrated 95% of the total variance shape and the first three modes explained 79% of the total variance shape. (b) Representation of the first 5 PLS deformation modes.*

Figure 3.7(b) illustrates the first 5 modes take into account. Like PCA, the first three modes describe the most shape variability (size, inclination and length of the neck). In particular, in table 3.8 is observable that the HAL parameters has more correlation in mode 3 and 4 than in the other three (mode 3: $R = 0.39$, $p = 0.000079$, mode 4: $R = -0.37$, $p = 0.000198$), while NSA is correlated with 4 modes (mode 1: $R = 0.21$, $p = 0.044$, mode 2: $R = 0.38$, $p = 0.00014$, mode 3: $R = -0.53$, $p = 0.000000034$, mode 4: $R = 0.28$, $p = 0.0056$).

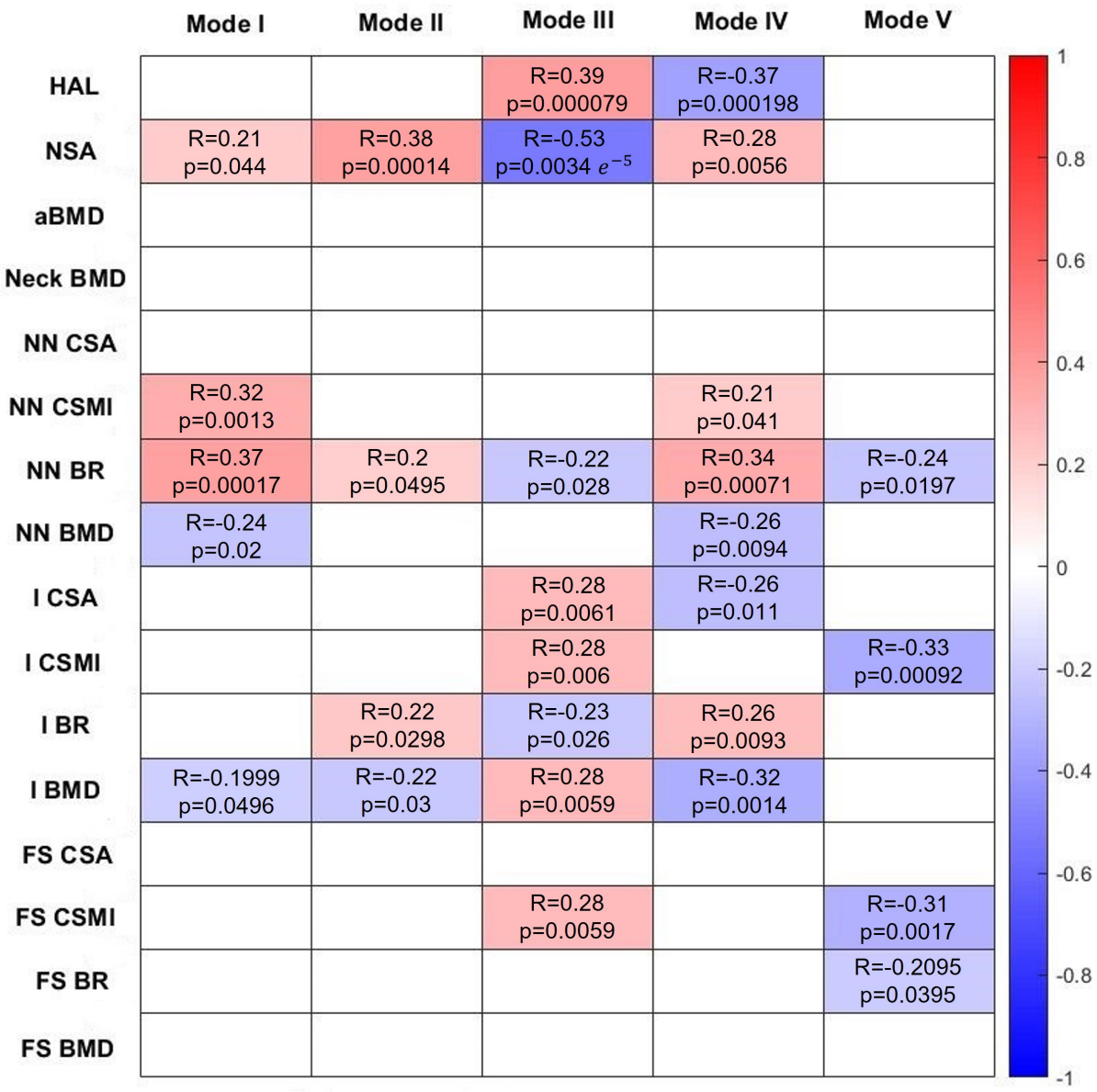

Figure 3.8: *Correlation Matrix Plot of PLS mode and HSA parameters*

The capability of PCA and PLS components to determine hip fracture status is brought out in figure 3.9, where the components are presented in the space represented by the first two and three modes for shape. By a visual inspection emerge that the capability of PLS in differentiating fracture subjects and non-fracture one is more marked than that of PCA components.

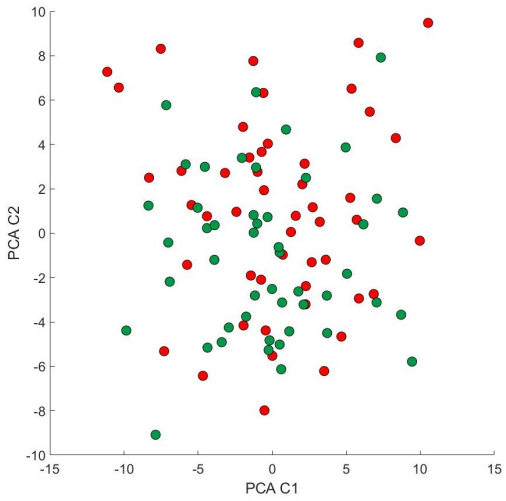

(a) *PCA 2D scatter plot*

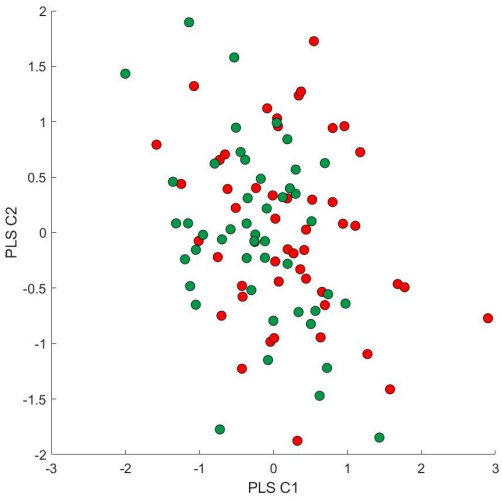

(b) *PLS 2D scatter plot*

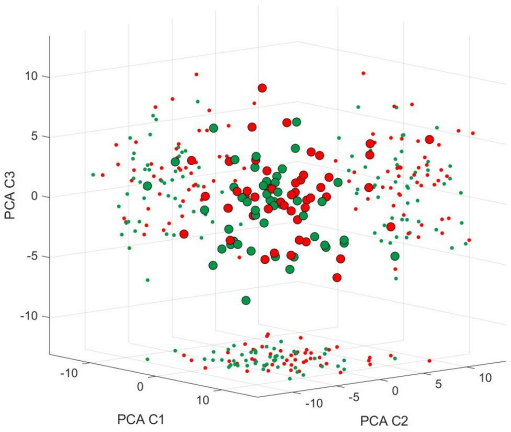

(c) *PCA 3D scatter plot*

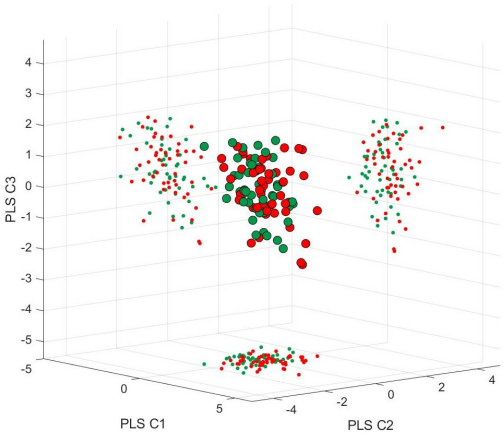

(d) *PLS 3D scatter plot*

Figure 3.9: *Scatter plots of the PCA and PLS components corresponding to the first two (a-b) and three (c-d) modes for the SSM. The PCA and PLS components of the fractured and non-fractured subjects are shown in red and green in order. The plot refers to the statistical shape models built on the full cohort.*

3.3 Prediction model

After a random division of the dataset into 10 distinct groups, a logistic regression model was executed on the first two, three, four and five components of both PCA and PLS. A first visual analysis of the ROC curves (figure 3.10) shows that PLS has more sensitivity than PCA; in particular the AUC for the PLS are settled between 0.62 and 0.63, while those for the PCA are set between 0.59 and 0.62. An additional measure is the aBMD, the current gold standard for assessing the risk of hip fracture, whose AUC is 0.73. This means that PLS has a better diagnostic capability than PCA but does not exceed the current gold standard.
The confusion matrices associated to the 10-fold cross-validation procedure for patient classification are provided in figure 3.11.

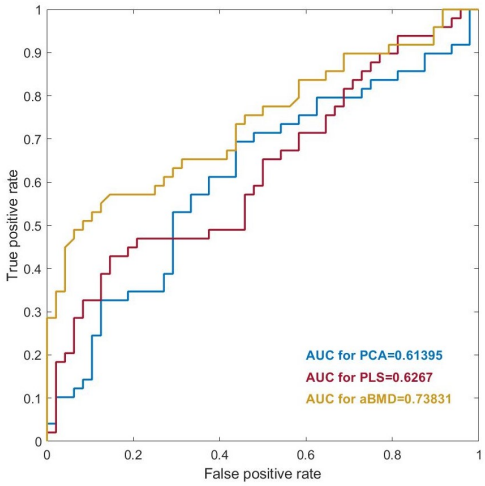

(a) *Two components of PCA and PLS*

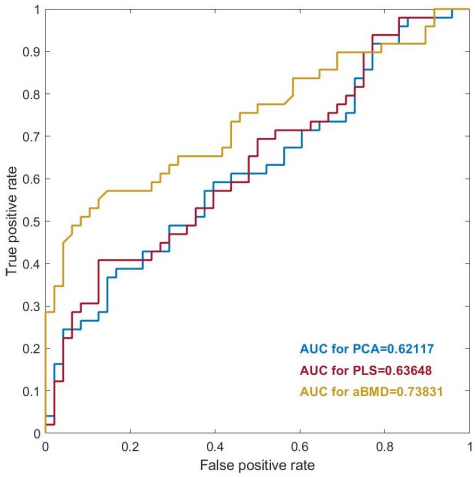

(b) *Three components of PCA and PLS*

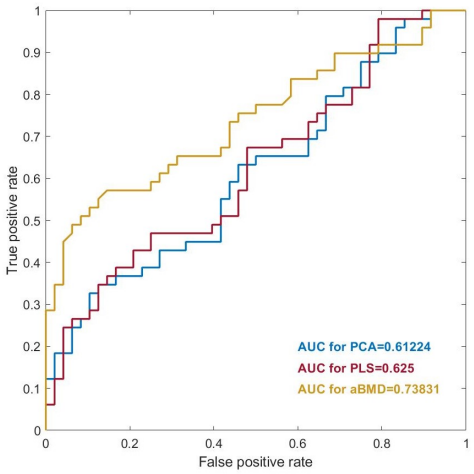

(c) *Four components of PCA and PLS*

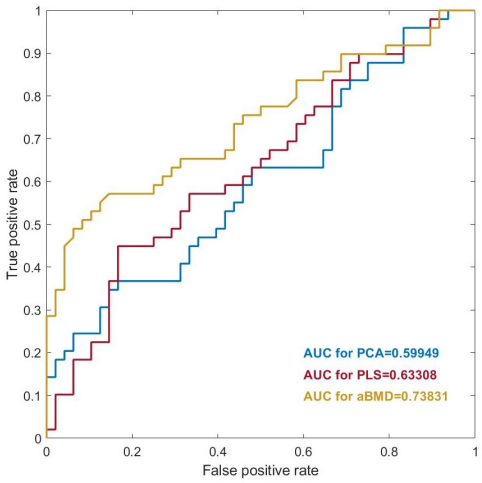

(d) *Five components of PCA and PLS*

Figure 3.10: *ROC curve and their relative AUC for the first (a) two components, (b) three components, (c) four components and (d) five components*

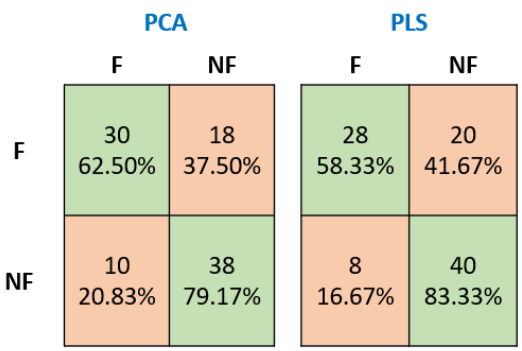

(a) *Two components SSM-based model*

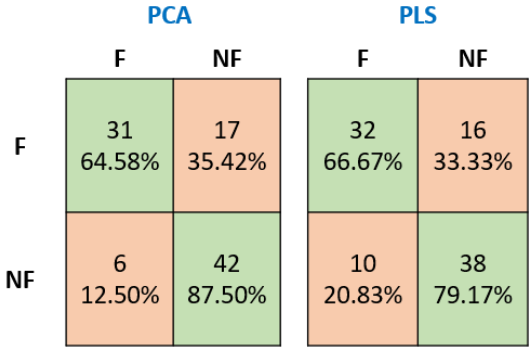

(b) *Three components SSM-based model*

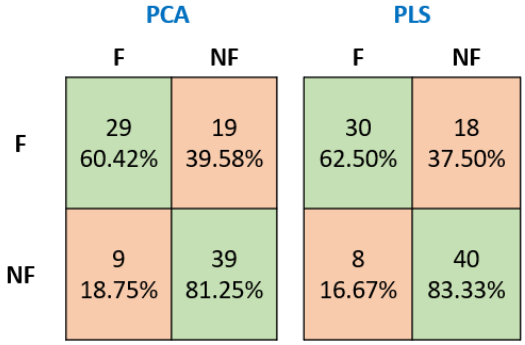

(c) *Four components SSM-based model*

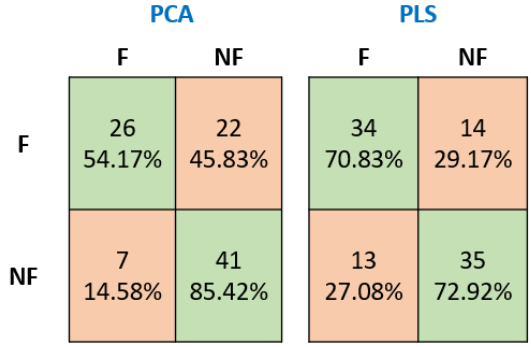

(d) *Five components SSM-based model*

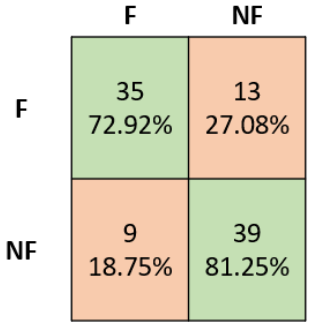

(e) *BMD-based model*

Figure 3.11: *Confusion matrix related to the classification of the patient as fractured (F) or non-fractured (NF) for the SSM and BMD-based regression models.*

4. Conclusions

Due to the constant increase in life expectancy, the relative rise in the incidence of hip fractures, and the limited sensitivity of the T-score in assessing the risk of fracture, many authors have put their attention to the search for an improved method for its prediction [5, 27, 36, 37, 42, 48].

In this study the use of statistical shape models, derived from DXA imges, was assessed, that allowed a better prediction of the fracture than the current gold standard.
Two methodologies, PCA and PLS, were used to create such SSMs. The main difference found is that PCA delivered more significant features in terms of geometry and features that reveal most of the variability in the intake population than PLS, consistent with the fact that PCA derives the characteristics that are optimal for representing the information; while PLS allows deriving the main shape features more subject to fracture, as it also takes into account the state of fracture. The use of two information allowed PLS to have better discriminating power.
The discriminating power of the two methods has been tested using logistic regression models. Through the analysis of ROC curves, it was observed that the discriminating power of PCA-based SSM was lower than PLS-based SSM and the latter was lower than the current gold standard based on aBMD. Therefore, the use of only the shape characteristics does not allow to predict adequately the risk of fracture, presenting a lower AUC than the aBMD.

It is also important to note that several limitations may have influenced the work presented here, such as the inaccuracy of the DXA technique and the possible inaccuracy of the positioning of the leg (If the leg is not in the proper position, the DXA image may have incorrect geometry information). Moreover, since DXA is a projective technique, the head region had a high density, this did not allow to have the precise shape of the head but it was simplified as a circle. In addition to this, the patient's history has not been taken into account and therefore factors such as alcohol, tobacco or medication consumption, which lead to bone variation, have not been considered.

In conclusion, the results of this study demonstrate the dominance of PLS to PCA during classification but do not explain an improvement in prediction compared to the current gold standard. The inclusion of Statistical Intensity Models (SIMs), built starting from the local BMD values of DXA images, might allow an enhanced fracture risk assessment.

Bibliography

[1] G. Anastasi et al. *Trattato di anatomia umana sistematica e funzionale - volume 1*. Milano: Edi.Ermes s.r.l., 2020.

[2] Musumeci C. *Analisi a elementi finiti 2D del femore prossimale: verifica dell'attendibilità del rischio di frattura osteoporotica tramite confronto con modelli 3D*. 2018.

[3] Seeley; Stephens; Tate. *Anatomia - 2th edizione*. Idelson-Gnocchi.

[4] Aldieri A. *Fracture Risk of the Proximal Femur in Osteoporosis: a Closer Look at the Role of Geometry*. 2020.

[5] WHO Study Group. "Assessment of fracture risk and its application to screening for postmenopausal osteoporosis". In: *WHO Technical Report Series* (1994).

[6] M. L. Brandi; G. Guglielmi; S. Masala; S. Minisola; F. Oleari; S. Ortolani; F. Palumbo; P. Pisanti; G. Simonetti; U. Tarantino; R. Ugenti. "Appropriatezza diagnostica e terapeutica nella prevenzione delle fratture da fragilità da osteoporosi". In: *Quaderni del Ministero della Salute* (2010). URL: http://www.quadernidellasalute.it.

[7] Eastell R; Walsh JS; Watts NB; Siris E. "Bisphosphonates for postmenopausal osteoporosis". In: *Bone* (2011). DOI: 10.1016/j.bone.2011.02.011.

[8] Lia Mara Montagner Rossi; Rafaela Martinez Copes; Leo Canterle Dal Osto; Clovis Flores; Fábio Vasconcellos Comim; Melissa Orlandin Premaor. "Factors related with osteoporosis treatment in post-menopausal women". In: *Medicine* (2018). DOI: http://dx.doi.org/10.1097/MD.0000000000011524.

[9] Yanlin Su; Zhe Chen; and Wei Xie. "Swimming as Treatment for Osteoporosis: A Systematic Review and Meta-analysis". In: *BioMed Research International* (2020). DOI: https://doi.org/10.1155/2020/6210201.

[10] Rossini M; Adami S; Bertoldo F; Diacinti D; Gatti D; Giannini S; Giusti A; Malavolta N; Minisola S; Osella G; Pedrazzoni M; Sinigaglia L; Viapiana O; Isaia GC. "Guidelines for the diagnosis, prevention and management of osteoporosis". In: *Reumatismo.* (2016). DOI: 10.4081/reumatismo.2016.870.

[11] Ström O; Borgström F; Kanis JA; Compston J; Cooper C; McCloskey EV; Jönsson B. "Osteoporosis: burden, health care provision and opportunities in the EU". In: *Pharmaceutical Industry Associations (EFPIA). Arch Osteoporos.* (2011). DOI: 10.1007/s11657-011-0060-1.

[12] Hernlund E; Svedbom A; Ivergård M; Compston J; Cooper C; Stenmark J; McCloskey EV; Jönsson B; Kanis JA. "Osteoporosis in the European Union: medical management, epidemiology and economic burden". In: *Arch Osteoporos.* (2013). DOI: 10.1007/s11657-013-0136-1.

[13] J.A. Kanis; C. Cooper; R. Rizzoli; J.-Y. Reginster. "European guidance for the diagnosis and management of osteoporosis in postmenopausal women". In: *Osteoporosis international* (2020). DOI: https://doi.org/10.1007/s00198-018-4704-5.

[14] Qiaozhen Zhou; Li Zhu; Dafeng Zhang; Ning Li; Qiao Li; Panpan Dai; YixinMao; Xumin Li; Jianfeng Ma; and Shengbin Huang. "Oxidative Stress-Related Biomarkers in Postmenopausal Osteoporosis: A Systematic Review and Meta-Analyses". In: *Hindawi Publishing Corporation* (2016). DOI: http://dx.doi.org/10.1155/2016/7067984.

[15] *Osteoporosi.* URL: https://art.torvergata.it/retrieve/handle/2108/993/5516/tesi.pdf.

[16] Brandi M. L.; Di Medio L. "Osteoporosi. Update diagnosi, follow-up e terapia". In: *Fondazione onda* (2019).

[17] Iwamoto J; Sato Y; Takeda T; Matsumoto H. "Whole body vibration exercise improves body balance and walking velocity in postmenopausal osteoporotic women treated with alendronate: Galileo and Alendronate Intervention Trail (GAIT)". In: *J Musculoskelet Neuronal Interact.* (2012).

[18] Aldieri A; Terzini M; Audenino A L; Bignardi C; Morbiducci U. "Combining shape and intensity dxa-based statistical approaches for osteoporotic HIP fracture risk assessment". In: *Computers in Biology and Medicine* (2020). DOI: https://doi.org/10.1016/j.compbiomed.2020.104093.

[19] Larson DR. Melton LJ 3rd Therneau TM. "Long-term trends in hip fracture prevalence: the influence of hip fracture incidence and survival." In: *Osteoporos Int.* (1998). DOI: 10.1007/s001980050050..

[20] Roche JJ; Wenn RT; Sahota O; Moran CG. "Effect of comorbidities and postoperative complications on mortality after hip fracture in elderly people: prospective observational cohort study." In: *BMJ* (2005). DOI: 10.1136/bmj.38643.663843.55.

[21] Diab DL; Watts NB. "Postmenopausal osteoporosis". In: *Curr Opin Endocrinol Diabetes Obes* (2013). DOI: 10.1097/01.med.0000436194.10599.94..

[22] *Mineralometria ossea computerizzata e densitometria ossea.* URL: https://www.bonehealth.it/mineralometria-ossea-computerizzata-e-densitometria/.

[23] "Individuazione dei criteri di Accesso alla Densitometria Ossea". In: *Ministero della salute* (2005). URL: https://www.salute.gov.it/imgs/C_17_pubblicazioni_1171_allegato.pdf.

[24] Capuani S; Manenti G; Iundusi R; Tarantino U. "Il ruolo della risonanza magnetica nella diagnosi di osteoporosi". In: *BioMed Res Int* (2015). DOI: http://dx.doi.org/10.1155/2015/948610.

[25] Tristan Whitmarsh; Ludovic Humbert; Mathieu De Craene; Luis M. del Río Barquero; Karl Fritscher; Rainer Schubert; Felix Eckstein; Thomas Link; and Alejandro F. Frangi. "3D bone mineral density distribution and shape reconstruction of the proximal femur from a single simulated DXA image: an in vitro study". In: *Medical Imaging* (2010). DOI: https://doi.org/10.1117/12.844110.

[26] F. Jazinizadeh; J.D. Adachi; C.E. Quenneville. "Advanced 2D image processing technique to predict hip fracture risk in an older population based on single DXA scans". In: *Osteoporosis International* (2020). DOI: https://doi.org/10.1007/s00198-020-05444-7.

[27] Beck TJ. "Extending DXA Beyond Bone Mineral Density: Understanding Hip Structure Analysis". In: *Curr Osteoporos Rep* (2007). DOI: 10.1007/s11914-007-0002-4.

[28] C J Gibson. "Medical radiation dose issues associated with dual-energy X-ray absorptiometry (DXA) scans for sports performance assessments and other non-medical practices". In: *COMARE)* (2019).

[29] R.M. Lorente Ramos; J. Azpeitia Armán; N. Arévalo Galeano; A. Mu˜noz Hernández; J.M. García Gómez; J. Gredilla Molinero. "Dual energy X-ray absorptimetry: Fundamentals, methodology, and clinical applications". In: *Radiologìa* (2011).

[30] Morris et al. “High-Spatial-Resolution Bone Densitometry with Dual-Energy X-ray Absorptiometric Region-free Analysis”. In: *Radiology* (2015). DOI: 10.1148/radiol.14140636.

[31] Harvey N; Dennison E; Cooper C. “Osteoporosis: impact on health and economics”. In: *Nat Rev Rheumatol* (2010). DOI: https://doi.org/10.1038/nrrheum.2009.260.

[32] Sanford Baim. “Assessment of Fracture Risk”. In: *Rheum Dis Clin* (2011). DOI: 10.1016/j.rdc.2011.07.001.

[33] Stacey A. Wainwright; Lynn M. Marshall; Kristine E. Ensrud; Jane A. Cauley; Dennis M. Black; Teresa A. Hillier; Marc C. Hochberg; Molly T. Vogt; Eric S. Orwoll. “Hip Fracture in Women without Osteoporosis”. In: *The Journal of Clinical Endocrinology and Metabolism* (2005). DOI: https://doi.org/10.1210/jc.2004-1568.

[34] Kanis J; McCloskey E; Johansson H et al. “Approaches to the targeting of treatment for osteoporosis”. In: *Nat Rev Rheumatol* (2009). DOI: https://doi.org/10.1038/nrrheum.2009.139.

[35] Sanford Baim; William D. Leslie. “Assessment of Fracture Risk”. In: *Curr Osteoporos Rep* (2012). DOI: 10.1007/s11914-011-0093-9.

[36] Cooper C; Atkinson EJ; Jacobsen SJ; O’Fallon WM; Melton LJ 3rd. “Population-based study of survival after osteoporotic fractures”. In: *Am J Epidemiol* (1993). DOI: 10.1093/oxfordjournals.aje.a116756.

[37] Gregory JS; Aspden RM. “Femoral geometry as a risk factor for osteoporotic hip fracture in men and women”. In: *Med Eng Phys* (2008). DOI: 10.1016/j.medengphy.2008.09.002.

[38] Beck TJ; Broy SB. “Measurement of Hip Geometry-Technical Background”. In: *J Clin Densitom* (2015). DOI: 10.1016/j.jocd.2015.06.006.

[39] Terzini M; Aldieri A; Rinaudo L; Osella G; Audenino AL; Bignardi C. “Improving the Hip Fracture Risk Prediction Through 2D Finite Element Models From DXA Images: Validation Against 3D Models”. In: *Front Bioeng Biotechnol* (2019). DOI: 10.3389/fbioe.2019.00220.

[40] S Gnudi; E Sitta; E Pignotti. “Prediction of incident hip fracture by femoral neck bone mineral density and neck–shaft angle: a 5-year longitudinal study in post-menopausal females”. In: *The British journal of radiology* (2012). DOI: 10.1259/bjr/57130600.

[41] Stephen Kaptoge; Thomas J Beck; Jonathan Reeve; Katie L Stone; Teresa A Hillier; Jane A Cauley; Steven R Cummings. “Prediction of incident hip fracture risk by femur geometry variables measured by hip structural analysis in the study of osteoporotic fractures”. In: *Journal of Bone and Mineral Research* (2008). DOI: 10.1359/jbmr.080802.

[42] M Di Stefano; GC Isaia; D Cussa; GL Panattoni. “Preliminary results on trabecular bone score (TBS) in lumbar vertebrae with experimental altered microarchitecture”. In: *J. Biol. Res* (2013). DOI: https://doi.org/10.4081/jbr.2013.3667.

[43] Casabella A; Seriolo C; Botticella G; Molfetta L. “Trabecular bone score (TBS): innovativo parametro di valutazione ossea nelle patologie reumatiche”. In: *Giornale Italiano di Ortopedia e Traumatologia* (2016).

[44] Schileo E; Taddei F; Cristofolini L; Viceconti M. “Subject-specific finite element models implementing a maximum principal strain criterion are able to estimate failure risk and fracture location on human femurs tested in vitro”. In: *J Biomech* (2008). DOI: 10.1016/j.jbiomech.2007.09.009.

[45] Bhattacharya P; Altai Z; Qasim M; Viceconti M. “A multiscale model to predict current absolute risk of femoral fracture in a postmenopausal population”. In: *Biomech Model Mechanobiol* (2019). DOI: 10.1007/s10237-018-1081-0.

[46] Luo Y; Ferdous Z; Leslie WD. "A preliminary dual-energy X-ray absorptiometry-based finite element model for assessing osteoporotic hip fracture risk". In: *Proc Inst Mech Eng H* (2011). DOI: 10.1177/0954411911424975.

[47] Masoud Nasiri Sarvi; Yunhua Luo. "A Two-Level Subject-Specific Biomechanical Model for Improving Prediction of Hip Fracture Risk". In: *Clinical Biomechanics* (2015). DOI: 10.1016/j.clinbiomech.2015.05.013.

[48] Schuler B; Fritscher KD; Kuhn V; Eckstein F; Link TM; Schubert R. "Assessment of the individual fracture risk of the proximal femur by using statistical appearance models". In: *Med Phys* (2010). DOI: 10.1118/1.3425791.

[49] Zhang J; Besier TF. "Accuracy of femur reconstruction from sparse geometric data using a statistical shape model". In: *Comput Methods Biomech Biomed Engin* (2017). DOI: 10.1080/10255842.2016.1263301.

[50] Sarkalkan N; Weinans H; Zadpoor AA. "Statistical shape and appearance models of bones". In: *Bone* (2014). DOI: 10.1016/j.bone.2013.12.006.

[51] Wang J; Shi C. "Automatic construction of statistical shape models using deformable simplex meshes with vector field convolution energy". In: *BioMed Eng OnLine* (2017). DOI: https://doi.org/10.1186/s12938-017-0340-0.

[52] Isaac Castro-Mateos; Jose M Pozo; Timothy F Cootes; J Mark Wilkinson; Richard Eastell; Alejandro F Frangi. "Statistical shape and appearance models in osteoporosis". In: *Current osteoporosis reports* (2014). DOI: 10.1007/s11914-014-0206-3.

[53] Reyneke Cornelius; Thusini Xolisile; Douglas Tania; Vetter Thomas; Mutsvangwa Tinashe. "Construction and validation of image-based statistical shape and intensity models of bone". In: *2018 3rd Biennial South African Biomedical Engineering Conference (SAIBMEC)* (2018). DOI: 10.1109/SAIBMEC.2018.8363176.

[54] Yang L; Udall WJ; McCloskey EV; Eastell R. "Distribution of bone density and cortical thickness in the proximal femur and their association with hip fracture in postmenopausal women: a quantitative computed tomography study". In: *Osteoporos Int.* (2014). DOI: 10.1007/s00198-013-2401-y.

[55] Stanley Durrleman; Marcel Prastawa; Nicolas Charon; Julie R. Korenberg; Sarang Joshi; Guido Gerig; Alain Trouvé. "Morphometry of anatomical shape complexes with dense deformations and sparse parameters". In: *NeuroImage* (2014). DOI: http://dx.doi.org/10.1016/j.neuroimage.2014.06.043.

[56] Durrleman S. "Statistical models of currents for measuring the variability of anatomical curves, surfaces and their evolution". In: *Phd Thesis* ().

[57] Durrleman S; Pennec X; Trouvé A; Thompson P; Ayache N. "Inferring brain variability from diffeomorphic deformations of currents: an integrative approach". In: *Med Image Anal.* (2008). DOI: 10.1016/j.media.2008.06.010.

[58] Durrleman S; Pennec X; Trouvé A; Ayache N. "Statistical models of sets of curves and surfaces based on currents". In: *Med Image Anal.* (2009). DOI: 10.1016/j.media.2009.07.007.

[59] *Analisi di sensitività, sensitività, calibrazione*. URL: https://studylibit.com/doc/748582/analisi-di-sensitivit%C3%A0--sensitivit%C3%A0--calibrazione-calibra....

[60] *Analisi della sensibilità per ciò che funziona, come farlo ed esempio*. URL: https://it.thpanorama.com/blog/administracion-y-finanzas/anlisis-de-sensibilidad-para-qu-sirve-cmo-hacerlo-y-ejemplo.html.

[61] *Deformetrica's documentation*. URL: https://gitlab.com/icm-institute/aramislab/deformetrica/-/wikis/home.

[62] Bôney A; Louisy M; Martin B; Durrleman S. "Deformetrica 4: An Open-Source Software for Statistical Shape Analysis". In: *ResearchGate* (2018). DOI: 10.1007/978-3-030-04747-4_1.

[63] Bruse JL; McLeod K; Biglino G; Ntsinjana HN; Capelli C; Hsia TY; Sermesant M; Pennec X; Taylor AM; Schievano S; Modeling of Congenital Hearts Alliance (MOCHA) Collaborative Group. "A statistical shape modelling framework to extract 3D shape biomarkers from medical imaging data: assessing arch morphology of repaired coarctation of the aorta". In: *BMC Medical Imaging* (2016). DOI: 10.1186/s12880-016-0142-z.

[64] Ambellan F; Lamecker H; von Tycowicz C; Zachow S. "Statistical Shape Models: Understanding and Mastering Variation in Anatomy". In: *Biomedical Visualisation. Advances in Experimental Medicine and Biology, vol 1156. Springer, Cham.* (2019). DOI: https://doi.org/10.1007/978-3-030-19385-0_5.

[65] Jolliffe IT; Cadima J. "Principal component analysis: A review and recent developments". In: *Philos Trans A Math Phys Eng Sci* (2016). DOI: 10.1098/rsta.2015.0202.

[66] Markus Ringnér. "What is principal component analysis?" In: *Nat Biotechnol* (2008). DOI: https://doi.org/10.1038/nbt0308-303.

[67] Jolliffe IT. *Principal Component Analysis, second edition.* Sprinher, 2020.

[68] Aldieri A; Bhattacharya P; Paggiosi M; Eastell R; Audenino AL; Bignardi C; Morbiducci U; Terzini M. "mproving the Hip Fracture Risk Prediction with a Statistical Shape-and-Intensity Model of the Proximal Femur". In: *Annals of Biomedical Engineering* (2022). DOI: 10.1007/s10439-022-02918-z.

Ringraziamenti

A conclusione di questo elaborato, mi sento in dovere di dedicare questo spazio a tutte le persone che mi hanno sostenuto in questo lungo percorso universitario.

Prima di tutto vorrei ringraziare la Dr. Alessandra Aldieri, Co-relatrice di questa tesi, per la sua immensa pazienza, per i suoi consigli e per avermi guidato passo passo in questa prima esperienza nel mondo della ricerca.

Ringrazio la Dr. Mara Terzini, relatrice di questa tesi, per avermi dato l'opportunità di svolgere il lavoro presentato qui.

Ringrazio infinitamente i miei sponsor, mia madre e mio padre, che senza il loro sostegno e incoraggiamento oggi non sarei qui a festeggiare questo traguardo. Ringrazio anche mio fratello che non è fuggito ogniqualvolta lo chiamassi per ripetere. Non finirò mai di ringraziarvi per avermi permesso di arrivare fin qui.

Devo ringraziare anche i miei amici di Università e di sempre che mi hanno sopportato/supportato durante questi 5 anni, che ogni giorno hanno condiviso con me gioie, sacrifici e successi, ma soprattutto gelati in pieno inverno. Grazie per aver ascoltato i miei sfoghi e grazie per tutti i momenti di spensieratezza.

Per ultimo ma non meno importante, vorrei ringraziare il mio ragazzo che in questi 6 mesi di tesi è riuscito sempre a darmi man forte, a farmi uscire e svagare, ad aver risolto i miei dubbi in tarda sera su quale risultato fosse migliore nonostante non conoscesse l'argomento. Grazie per tutto il tempo che mi hai dedicato.

A tutti Grazie per esserci stati.